Analysis of Photonic Crystal Filters
by the Finite-Difference Time-Domain Technique

by

Bae-Ian Wu

B.Eng. Electronic Engineering
The Chinese University of Hong Kong, 1997

Submitted to the Department of Electrical Engineering and Computer Science
in partial fulfillment of the requirements for the degree of
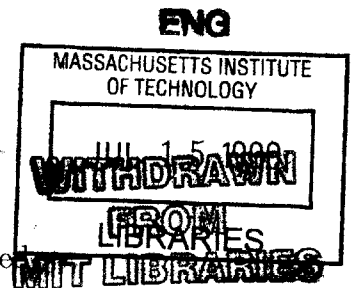
Master of Science

at the

MASSACHUSETTS INSTITUTE OF TECHNOLOGY

May 1999

[June 1999]

Author ....
Department of Electrical Engineering and Computer Science
May 24, 1999

Certified by...
Dr. Jin Au Kong
Professor of Electrical Engineering
Thesis Supervisor

Certified by...
Dr. Y. Eric Yang
Research Scientist
Thesis Supervisor

Accepted by...
Arthur C. Smith
Chairman, Department Committee on Graduate Students

Analysis of Photonic Crystal Filters

by the Finite-Difference Time-Domain Technique

by

Bae-Ian Wu

Submitted to the Department of Electrical Engineering and Computer Science
on May 24, 1999, in partial fulfillment of the
requirements for the degree of
Master of Science

Abstract

A special finite-difference time-domain (FD-TD) formulation which allows electromagnetic (EM) wave wideband simulations of oblique incidence for periodic media is used for the design and analysis of an infrared photonic crystal filter with dual stopbands at $3 - 5\,\mu$m and $8 - 12\,\mu$m. The transmission coefficient in the main stopband $(8 - 12\,\mu$m) is below $-10\,$dB. Scattering coefficients are calculated for different incidence angles, and the stopbands are shown to exist for different angles of incidence.

A hybrid method is developed for analyzing multilayer structures. Scattering coefficients from a single layer filter can be computed by using FD-TD. Applying microwave network theory, the scattering characteristics of a single layer can be represented by a generalized scattering matrix which can be transformed into a transfer matrix. Scattering by multilayer structures is then calculated by the multiplication of transfer matrices. This technique allows efficient analysis of different configurations of layers without resorting to full EM simulation, which requires a lot of computing time and memory. Using the hybrid method, the transmission coefficients of cascaded metal screens with different angles of incidence are presented and compared with FD-TD results. The contributions of higher-order modes to the transmission characteristics are identified.

Thesis Supervisor: Dr. Jin Au Kong
Title: Professor of Electrical Engineering

Thesis Supervisor: Dr. Y. Eric Yang
Title: Research Scientist

Acknowledgments

To my parents, my brother and Mimi

Contents

List of Figures

List of Tables

Chapter 1

Introduction

Photonic crystals [1, 2] are a class of photonic devices that utilize periodic structures to create photonic band gaps [3, 1], analogous to the III-V compound semiconductors in which photons with specific energies cannot be transmitted through the structures. The periodicity of photonic crystals can be formed by differences in dielectric constant, or by a combination of metal and dielectric, and hence the term metallodielectric photonic crystals (MDPC) [4].

Analysis of photonic crystal filters is similar to yet different from the analysis of frequency selective surfaces (FSS). It is because the close coupling between the periodic elements make it more difficult to predict the scattering characteristics. To design an IR filter using photonic crystals, experimental and theoretical techniques can be used. However, the cost and time for fabrication and testing become prohibitively high. An accurate electromagnetic model is in demand.

Applications of photonic crystal filters have been found in several areas. For thermal sensors, they can be used to isolate the interference from the atmospheric background. With dichroic plates [5], incident electromagnetic waves with different frequencies can be separated at large angle of incidence. In thermophotovoltaic (TPV)
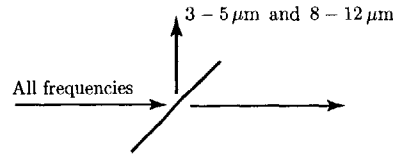
Figure 1-1: Usage of photonic crystal filter as a sensor window.

cells, it improves the efficiency of the cell by providing spectral control of the emission from the thermal source. There are numerous applications where dichroic filters that operate over a wide solid angle are desirable. Consider, for example, a satellite-based IR imager which maps the Earth's surface in the $3 - 4\,\mu m$ and $8 - 12\,\mu m$ bands where the atmosphere is transparent. To minimize out-of-band loading of the IR sensor from the albedo, a useful primary mirror coating would reflect strongly from $3 - 4\,\mu m$ and $8 - 12\,\mu m$ and would transmit out-of-band radiation away from the sensor. Another potential application is for low-emissivity window treatments for energy-efficient buildings.

1.1 Motivation

Previous experimental results [4, 6] based on an implementation of MDPC have demonstrated promising results in these two bands. An accurate electromagnetic modeling and fast analyzing method become very important for designing and understanding multilayer structures. It has become available recently and is being applied to actual design process in this research.

1.2   Past Works and Research Description

Analysis of FSS had been carried out by Ulrich [7], and approximation formulas for the transmission and reflection coefficients of the fundamental modes along the propagation direction have been found for metal screens with simple geometry. More accurate formulas for metal grids can be found in [8]. Subsequent development of FSS resulted in a variety of element geometries and configurations of the filters for higher frequency bands.

Traditional FSS in the microwave regime offer a filtering effect at the expense of angular dispersion, which causes the scattering coefficients for different angles of incidence to be different. This is highly undesirable in applications where omnidirectional performance is required. An omnidirectional mirror has been reported in [9] using a cascade of dielectric materials, which can produce a single stopband. In order to create a dual stopband, a metallodielectric photonic crystal (MDPC) is used. In MDPC, strong coupling of different Floquet modes can create stopbands that are comparatively insensitive to the angle of incidence. The oblique-incidence FD-TD formulation by Veysoglu [10] and Kao [11] allows accurate wide-band calculation of the scattering characteristics of a periodic medium at different incidence angles. Designing dual-band photonic crystal filters with omnidirectional stopbands is thus made possible.

Analysis of large structures with different configurations requires large computational resources. The transfer matrix method adapted from microwave network theory [12] can be applied to model each layer of a multilayer structure as a multimode element. Coupling between different modes of a single layer can be represented by a scattering matrix. By transforming the scattering matrix into a transfer matrix that can be cascaded, the scattering characteristics of a multilayer structure can be calculated.

In this research, there are two objectives. First, an IR bandstop filter implemented with MDPC for the bands $3 - 4\,\mu$m and $8 - 12\,\mu$m is to be designed. Second, a hybrid method based on the FD-TD and transfer matrix method is used to analyze the scattering characteristics of multilayer photonic crystal filters and compare the results with full FD-TD simulations.

1.2.1 Design of a Photonic Crystal Bandstop Filter in the Band $3 - 4\,\mu$m and $8 - 12\,\mu$m

Parametric studies based on the designs from several references with the oblique incidence FD-TD computer codes based on [11] have been carried out to study the transmission characteristics at normal incidence in the desired bands. Designs with good dual-band performance were chosen for oblique incidence simulations. Effects of finite thickness metal and dielectrics with high permittivities are studied. The final design utilizes thin metallic disks embedded in a dielectric substrate with $\epsilon_r = 2.1$. Calculations have shown that the stopbands persist over $\pm 60°$. The final design is scheduled for fabrication and testing at Lincoln Laboratory in Summer, 1999.

1.2.2 Analysis of Multilayer Structures by Hybrid Method Based on FD-TD and Transfer Matrix Formulation

A photonic crystal filter can be modeled as alternating layers of homogeneous dielectrics and metal arrays. Each layer can be represented by a scattering matrix, where the elements of the matrix are the scattering coefficients of different modes. Using FD-TD, scattering coefficients of a metal screen for different Floquet modes can be obtained from spatial integration of field quantities over the spatial harmonics, while for the dielectric layers, scattering coefficients can be calculated analytically.

Since the scattering matrix describes the relationship between the incident fields and the scattered fields, it can be transformed to a transfer matrix. With the formulation of the transfer matrix method, multilayer results can be obtained by multiplying (cascading) the transfer matrices, which in turn is based on single layer FD-TD results. Calculations from the transfer matrix method can then be compared with a computationally intensive FD-TD simulation of the multilayer structures.

1.3 Outline of the Thesis

The thesis is divided into 6 chapters. Chapter 1 contains the background, motivation and the description of the research. Chapter 2 introduces the formulation of the oblique incidence FD-TD method as the simulation tool for filter design. In Chapter 3 the simulation results of a parametric study and the calculated performance of the final photonic crystal filter design are presented. Chapter 4 describes the formulation of the hybrid method and how it can be used to analyze multilayer filters and Chapter 5 shows the comparison between FD-TD and the hybrid method. Finally, Chapter 6 concludes the thesis with a description of possible future work.

Chapter 2

Finite-Difference Time-Domain Method

In this chapter, the formulation of the Finite-Difference Time-Domain (FD-TD) method for periodic surfaces is introduced for both the normal and oblique incidence case. Regular FD-TD for periodic surfaces can handle plane waves at normal incidence only. The oblique FD-TD method can handle an obliquely incident plane wave.

2.1 Regular FD-TD Method

2.1.1 Central Differencing and Propagation Equations

The Finite-Difference Time-Domain (FD-TD) method [13] is based on the discretization of Maxwell equations:

$$\nabla \cdot \overline{B} = 0 \ , \quad \nabla \times \overline{H} = \frac{\partial \overline{D}}{\partial t} + \overline{J}$$

16

$$\nabla \cdot \overline{E} = \rho \ , \qquad \nabla \times \overline{E} = -\frac{\partial \overline{B}}{\partial t} \tag{2.1}$$

The Maxwell equations in differential form for free space are:

$$-\mu_o \frac{\partial H_x}{\partial t} = \frac{\partial E_z}{\partial y} - \frac{\partial E_y}{\partial z} \qquad \epsilon_o \frac{\partial E_x}{\partial t} = \frac{\partial H_z}{\partial y} - \frac{\partial H_y}{\partial z}$$

$$-\mu_o \frac{\partial H_y}{\partial t} = \frac{\partial E_x}{\partial z} - \frac{\partial E_z}{\partial x} \qquad \epsilon_o \frac{\partial E_y}{\partial t} = \frac{\partial H_x}{\partial z} - \frac{\partial H_z}{\partial x}$$

$$-\mu_o \frac{\partial H_z}{\partial t} = \frac{\partial E_y}{\partial x} - \frac{\partial E_x}{\partial y} \qquad \epsilon_o \frac{\partial E_z}{\partial t} = \frac{\partial H_y}{\partial x} - \frac{\partial H_x}{\partial y} \tag{2.2}$$

The curl equations of (2.1) are used together with the following central differencing scheme:

$$\frac{\partial}{\partial x} f(x) \simeq \frac{f(x + \Delta x/2) - f(x - \Delta x/2)}{\Delta x} \tag{2.3}$$

Upon discretization over time and space, differential equations can be rewritten as difference equations:

$$H_{x(i,j+\frac{1}{2},k+\frac{1}{2})}^{n+\frac{1}{2}} = H_{x(i,j+\frac{1}{2},k+\frac{1}{2})}^{n-\frac{1}{2}}$$

$$-\frac{\Delta\tau}{\mu_o \Delta} \left\{ [E_{z(i,j+1,k+\frac{1}{2})}^n - E_{z(i,j,k+\frac{1}{2})}^n] + [E_{y(i,j+\frac{1}{2},k)}^n - E_{y(i+1,j+\frac{1}{2},k+1)}^n] \right\}$$

$$H_{y(i+\frac{1}{2},j,k+\frac{1}{2})}^{n+\frac{1}{2}} = H_{y(i+\frac{1}{2},j,k+\frac{1}{2})}^{n-\frac{1}{2}}$$

$$-\frac{\Delta\tau}{\mu_o \Delta} \left\{ [E_{x(i+\frac{1}{2},j,k+1)}^n - E_{x(i+\frac{1}{2},j,k)}^n] + [E_{z(i,j,k+\frac{1}{2})}^n - E_{z(i+1,j,k+\frac{1}{2})}^n] \right\}$$

$$H_{z(i+\frac{1}{2},j+\frac{1}{2},k)}^{n+\frac{1}{2}} = H_{z(i+\frac{1}{2},j+\frac{1}{2},k)}^{n-\frac{1}{2}}$$

$$-\frac{\Delta\tau}{\mu_o \Delta} \left\{ [E_{y(i+1,j+\frac{1}{2},k)}^n - E_{y(i,j+\frac{1}{2},k)}^n] + [E_{x(i+\frac{1}{2},j,k)}^n - E_{x(i+\frac{1}{2},j+1,k)}^n] \right\}$$

$$E_{x(i+\frac{1}{2},j,k)}^{n+1} = E_{x(i+\frac{1}{2},j,k)}^{n}$$

$$+\frac{\Delta\tau}{\epsilon_o \Delta} \left\{ [H_{z(i,j+\frac{1}{2},k+\frac{1}{2})}^n - H_{z(i,j-\frac{1}{2},k+\frac{1}{2})}^n] + [H_{y(i+\frac{1}{2},j,k-\frac{1}{2})}^n - H_{y(i+\frac{1}{2},j,k+\frac{1}{2})}^n] \right\}$$

$$E^{n+1}_{y(i,j+\frac{1}{2},k)} = E^n_{y(i,j+\frac{1}{2},k)}$$

$$+ \frac{\Delta\tau}{\epsilon_o\Delta}\left\{[H^n_{x(i,j+\frac{1}{2},k+\frac{1}{2})} - H^n_{x(i,j+\frac{1}{2},k-\frac{1}{2})}] + [H^n_{z(i-\frac{1}{2},j+\frac{1}{2},k)} - H^n_{z(i+\frac{1}{2},j+\frac{1}{2},k)}]\right\}$$

$$E^{n+1}_{z(i,j,k+\frac{1}{2})} = E^n_{z(i,j,k+\frac{1}{2})}$$

$$+ \frac{\Delta\tau}{\epsilon_o\Delta}\left\{[H^n_{y(i+\frac{1}{2},j,k+\frac{1}{2})} - H^n_{y(i-\frac{1}{2},j,k+\frac{1}{2})}] + [H^n_{x(i,j-\frac{1}{2},k+\frac{1}{2})} - H^n_{x(i,j+\frac{1}{2},k+\frac{1}{2})}]\right\}$$

$$(2.4)$$

Regular Yee's Cell

Figure 2-1: Yee's lattice for Regular Finite-Difference Time-Domain formulation.

The superscripts indicate the time steps and the subscripts indicate the coordinates of the field quantities. $\Delta\tau$ is the time stepping unit and Δ is the space stepping unit. The resulting difference equations are applied to the computational space, which is based on the Yee lattice (Figure 2-1a). As indicated in (2.4), the E fields are located on the edges of the cells and are updated when $t = n$, while the H fields are

computed at the center of the faces of the cells and are updated when $t = n + 1/2$. This leap-frogging method allows the time-marching of the E and H fields and forms the basis of the propagation of EM waves inside the computational domain.

2.1.2 Numerical Dispersion and Stability

To ensure numerical stability and reliability, the discretization process must satisfy several conditions. Consider the dispersion relation for free space:

$$\omega^2 \epsilon_o \mu_o = k_x^2 + k_y^2 + k_z^2 \tag{2.5}$$

where the phase velocity is $c = 1/\sqrt{\mu_o \epsilon_o}$. In the discretized domain, the dispersion equation [14] becomes:

$$\sin^2 \frac{\omega \Delta t}{\Delta} = \left(\frac{c_o \Delta t}{\Delta} \right) \left\{ \sin^2 \frac{k_x \Delta}{2} + \sin^2 \frac{k_y \Delta}{2} + \sin^2 \frac{k_z \Delta}{2} \right\} \tag{2.6}$$

To ensure a consistent numerical phase velocity in the computational domain, the spatial discretization should be small enough such as

$$\Delta \leq \frac{\lambda_{min}}{10} \tag{2.7}$$

which give a sampling rate higher than the standard Nyquist sampling rate. For the temporal discretization, we can consider the case of uniform gridding. In order to ensure that ω in (2.6) is positive, the Courant stability criterion must be enforced at all times:

$$\Delta t \leq \frac{\Delta}{\sqrt{3}c}$$
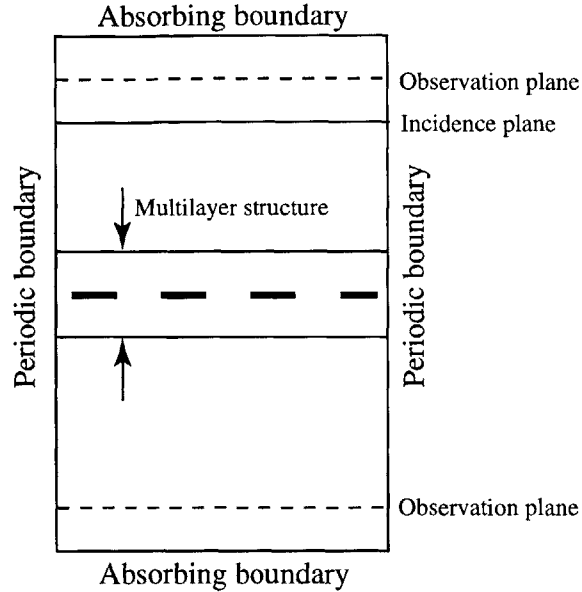
Figure 2-2: Cross section of the computational domain of FD-TD for periodic surfaces with absorbing boundary on top and bottom and periodic boundary at the sides.

2.1.3 Computational Domain

The computational domain is where the modeling of the filter is situated and the propagation and scattering are calculated. The cross section of the computational domain is shown in Figure 2-2. The top and bottom of the domain are terminated by absorbing boundaries and the sides are extended infinitely by imposing a periodic boundary condition. Inside the domain, the filter is in the middle of the computational column and the incidence plane where the incident plane wave is excited is above it. On top of the incidence plane, based on the "total-field/ scattered-field" formulation [14], only the scattered fields are calculated. The observation planes register the field quantities at every time step and through a temporal Fourier transform, the reflected and the transmitted fields at each sampled frequency can be calculated.

2.1.4 Modeling of Dielectrics and Conductors

Discontinuities of the propagation media in the computational domain are taken into consideration by different ways. In the presence of dielectric, the dielectric constant ϵ will be the average value of the different dielectric materials that share the same edge. Differences in permeabilities require a special treatment [11, 14] due to the discontinuities introduced in the H fields. In the analysis of photonic crystal filters, the substrates and metals will assume the value of μ_o.

Conducting elements in the filters are modeled as perfect electrical conductors and have to satisfy the boundary condition that the tangential electric field is zero on the surfaces of the metal: $\overline{E}_{\parallel} = 0$. This can be implemented by assigning zeros to the tangential electric fields of the metal object at the end of each time step.

2.1.5 Absorbing Boundary Condition

In order to simulate an infinite space in a finite computational domain, the top and bottom end are terminated by an absorbing boundary. Perfectly Matched Layer, or PML [15] is used as the absorbing boundary condition. It functions by creating computational layers with increasing electric and magnetic losses at the interfaces and is usually backed by a conductor. The incident waves will be attenuated to a small value before they are reflected. The reflected waves will be further attenuated to a level that usually will not interfere with the calculation of the scattered fields. The full PML equations based on the decomposition of the field quantities can be found in [11]. The matching of the successive layers is ensured by the following relation:

$$\frac{\sigma}{\sigma_m} = \frac{\epsilon}{\mu}$$
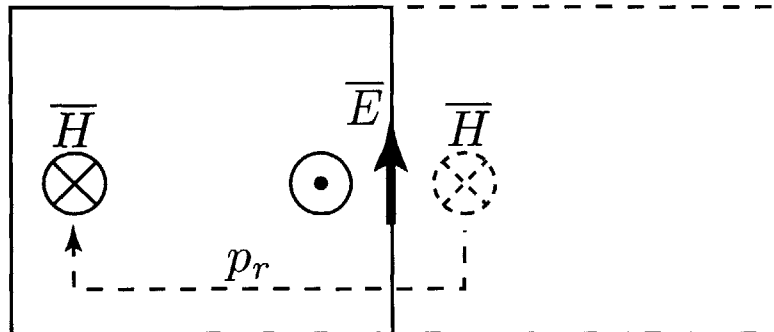
Figure 2-3: Periodic boundary condition. The field quantity outside the computational cell can be updated via translational symmetry.

Hence the name perfectly matched layer. Given an incident angle of θ_i, the reflection coefficient R of the PML can be expressed as:

$$R(\theta_i) = e^{-2\left(\frac{\cos\theta_i}{\epsilon_o c}\right) \int_0^{z_{max}} \sigma(z)dz}$$
(2.8)

where z_{max} is the total thickness of the absorbing layer and $\sigma(z)$ can be written as:

$$\sigma(z) = \sigma_{maz}\left(\frac{z}{z_{max}}\right)^n$$
(2.9)

Thus the absorption will depend on the maximum loss σ_{max}, the incidence angle θ_i and the order n of the PML. As the incidence angle θ_i approaches 90°, the PML effectively becomes a conductor. And waves incident to the PML at grazing angles will be reflected and interfere with the observation of the scattered fields.

2.1.6 Periodic Boundary Condition

The physical structure consists of the periodic elements, the computational domain, however, is reduced to only a unit cell size. In order to simulate the repetitive cells, a periodic boundary condition is used. Based on the condition that the field distribution on the surface is periodic, it can be expressed as:

$$\overline{H}(r, t) = \overline{H}(r + p_r, t) \tag{2.10}$$

where p_r is the periodicity of the structure. To apply this condition for the FD-TD code, first consider the electric field at the edge of the boundary (Figure 2-3). Take E_y as an example. To calculate E_y we need to know the value of H_z outside the boundary. But since the incident wave front is parallel to the surface (Figure 2-4a), by virtue of the periodic boundary condition, $\overline{H}(r, t) = \overline{H}(r + p_r, t)$. The periodicity is thus extended infinitely across the surface.

The situation is different for an obliquely incident wave (Figure 2-4b). The wave front is tilted and reach the surface at different times t. Since the validity of the operation (2.10) depend on the fact that the same phase front reaches the surface at the same time, the periodic boundary condition is no longer applicable in the case of oblique incidence. The updating process required an advanced field quantity and a non-causal situation is encountered:

$$\overline{H}(r, t_o) = \overline{H}(r + p_r, t_o + \Delta t) \tag{2.11}$$

To preserve the periodic boundary condition, a variable transformation of the fields is needed, which leads to the FD-TD formulation for oblique incidence.

(a)   (b)
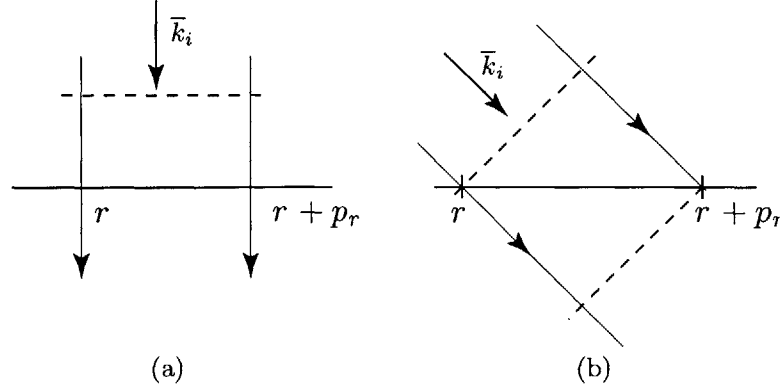
Figure 2-4: Comparison of wave front position between normal incidence and oblique incidence. Non-causal periodic boundary relation hinders the use of regular FD-TD for oblique incidence on periodic surfaces.

2.2 Oblique Incidence FD-TD

The oblique incidence formulation was first developed by Veysoglu [10], and Kao [11] derived the correct stability criteria and implemented them in the three-dimensional case. The method is based on adding a lateral phase shift to compensate the phase difference across the periodic surface so that the periodic boundary condition will causal again. In doing so, the Maxwell equations are changed to $\overline{P} - \overline{Q}$ differential equations, where $\overline{P}$ and $\overline{Q}$ are new field variable, replacing $\overline{E}$ and $\overline{H}$.

2.2.1 $P - Q$ Propagation Equations

Consider a plane wave at oblique incidence traveling in the $-z$ direction (Figure 2-5) with a wavevector $\overline{k}_i = \hat{x}k_x + \hat{y}k_y - \hat{z}k_z$:

$$\overline{E}_i = \overline{E}_o e^{ik_x x} e^{ik_y y} e^{-ik_z z} \tag{2.12}$$
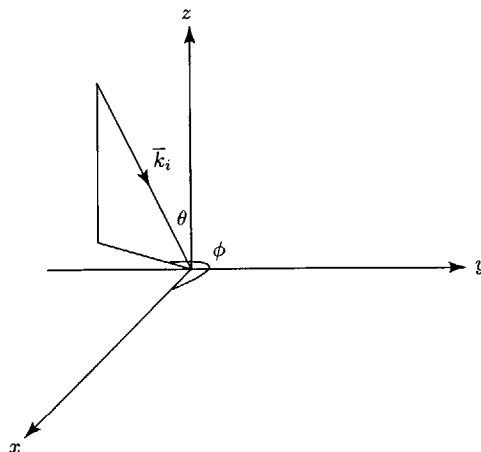
Figure 2-5: Orientation of $\overline{k}$-vector at oblique incidence.

Besides the dependence on z, the phase factor also depends on x and y. Define the lateral phase shift factor

$$e^{-i\overline{k}_l \cdot \overline{r}} = e^{-ik_x x} e^{-ik_y y}$$

with the lateral wavevector $\overline{k}_l$ to compensate the contribution from k_x and k_y. We can define new field variables $\overline{P}$ and $\overline{Q}$:

$$\overline{P} = \overline{E}_o e^{i\overline{k}_l \cdot \overline{r}} e^{-i\overline{k}_l \cdot \overline{r}} e^{-ik_z z}$$
$$\overline{Q} = \overline{H}_o e^{i\overline{k}_l \cdot \overline{r}} e^{-i\overline{k}_l \cdot \overline{r}} e^{-ik_z z} \tag{2.13}$$

Note that the lateral phase shift is removed and $\overline{P}$ and $\overline{Q}$ propagate normal to the surface although the vectors themselves are not parallel to the surface. It is not a plane wave, and will satisfy Maxwell equation only with the appropriate transformation of variables.

Rewriting Maxwell equations in the frequency domain for free space with $\overline{P}$ and $\overline{Q}$ gives:

$$\overline{k}_i' \times \overline{Q} + \overline{k}_l \times \overline{Q} = -\omega\epsilon_o\overline{P}$$
$$\overline{k}_i' \times \overline{P} + \overline{k}_l \times \overline{P} = \omega\mu_o\overline{Q} \tag{2.14}$$

where $\overline{k}_i' = \overline{k}_i - \overline{k}_l$ is the wavevector of the $\overline{P}$ and $\overline{Q}$. We can rewrite (2.14) in time domain as:

$$\nabla \times \overline{Q} = \frac{\partial}{\partial t}\left(\epsilon_o\overline{P} + \frac{\Lambda}{v} \times \overline{Q}\right)$$
$$\nabla \times \overline{P} = -\frac{\partial}{\partial t}\left(\mu_o\overline{Q} - \frac{\Lambda}{v} \times \overline{P}\right) \tag{2.15}$$

where

$$\Lambda = \hat{x}\sin\theta\cos\phi + \hat{y}\sin\theta\sin\phi \tag{2.16}$$

The equations (2.15) resemble the propagation of $\overline{E}$ and $\overline{H}$ in a bianisotropic medium [16]:

$$\nabla \times \overline{H} = \frac{\partial}{\partial t}\left(\epsilon_o\overline{E} + \overline{\overline{\xi}} \cdot \overline{H}\right)$$
$$\nabla \times \overline{E} = -\frac{\partial}{\partial t}\left(\mu_o\overline{H} + \overline{\overline{\zeta}} \cdot \overline{E}\right) \tag{2.17}$$

However, the $\overline{P}-\overline{Q}$ system is dispersive, as the corresponding ζ and ξ are not contants but are dependent on the angles of incidence θ and ϕ.

The subsequent difference equations are applied on the modified Yee's cell (Figure 2-6) which can also be considered as a superposition of regular Yee cells. The time stepping and the position of $\overline{P}$ and $\overline{Q}$ are shown in Figure 2-6.
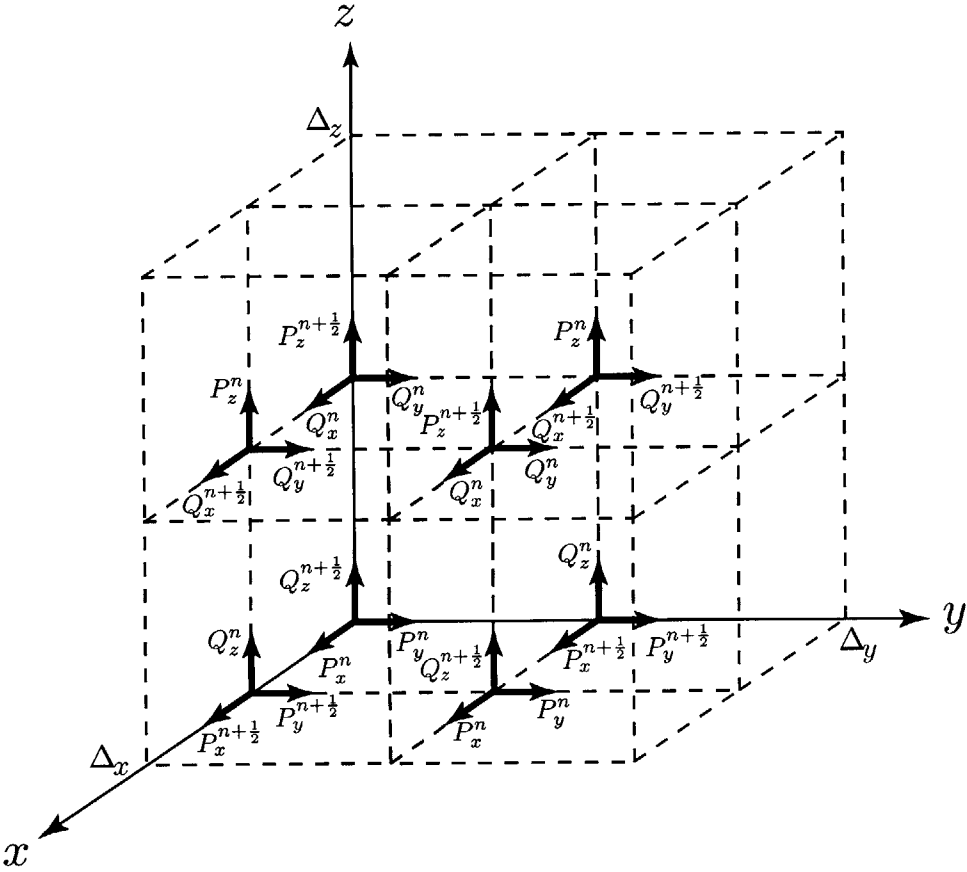
Figure 2-6: Modified Yee's lattice

2.2.2 Stability Criteria and Boundary Conditions

Stability Criteria

With the new $\overline{P} - \overline{Q}$ system, the stability criterion is also changed. Based on Kao's calculation [11]:

$$\frac{\Delta}{\Delta t} \geq \frac{v_i}{v_i^2 \mu \epsilon - \sin^2 \theta} \left\{ |\sin \theta \cos \phi| + |\sin \theta \sin \phi| + \sqrt{3 v_i^2 \mu \epsilon - 2 \sin^2 \theta \ (1 - |\sin \phi \cos \phi|)} \right\}$$

(2.18)

where v_i is the phase velocity of the incident wave on the incidence plane. For the upper limit on the right side, μ and ϵ are chosen to be the least dense material in the computational domain. Figure 2-7 shows the ratio between Δ and $c\Delta t$ as a function
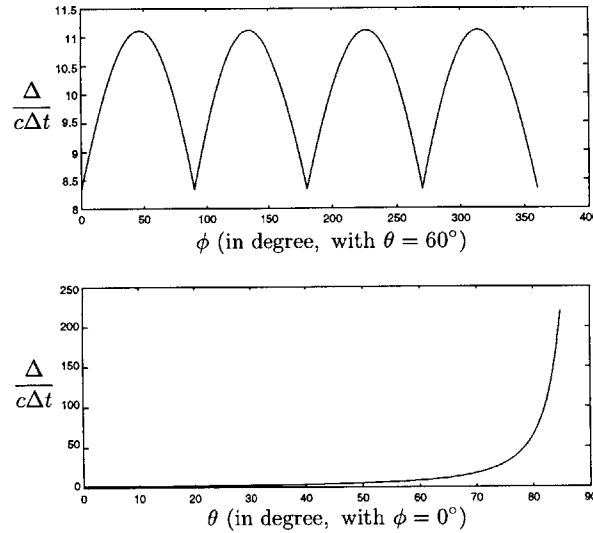
Figure 2-7: Ratio between Δ and $c\Delta t$ vs. θ and ϕ

of θ_i and ϕ. Along the azimuthal direction, this ratio has a four-fold symmetry and varies between minima (when the projection of $\overline{k}_i$ aligns with the x or y axis) and

maxima (when the projection of $\bar{k}_i$ is at 45° with the x or y axis). The same ratio $(\frac{\Delta}{c\Delta t})$ increase monotonically as the polar angle of incidence becomes larger. As $\theta_i \rightarrow 90°$, $\frac{\Delta}{c\Delta t} \rightarrow \infty$, and the time step Δt has to be infinitesimally small. On the other hand, as with the $\overline{P} - \overline{Q}$ differential equation, the stability criterion reduces to the Courant's stability criterion as the propagation vector of the incident wave become normal.

Boundary Condition

The periodic boundary condition of the $\overline{P} - \overline{Q}$ system is the same as in the case of normal incidence. Because of the finer grid, more field quantities are needed to be updated.

For the absorbing boundary conditions, the PML equations are changed in the same fashion as Maxwell equations. The lateral phase compensation is multiplied to the frequency domain equations before transforming back to the time domain.

The absorption of $\overline{P}$ and $\overline{Q}$ is similar to the normal incidence case. The simulations in this research are done with PML with 8 layers and the noise floor is below $-100\,\text{dB}$.

Chapter 3

Simulation Results and Analysis

In this chapter, the simulation results and the analysis of the infrared bandstop filters are presented. Firstly, the calculated transmission coefficient of a 3D MDPC filter with 3D elements is compared to the experimental results, which demonstrate the reliability of using FD-TD as a design tool for IR filter. Secondly, the structure and the geometry of the proposed filter is presented It is composed of three layers of periodic metal patches embedded in a dielectric. The normal incidence transmission characteristics of the proposed filter are studied by varying the different geometric parameters. The optimal design is further evaluated at different incidence angles. The effects of high permittivity and alignment are discussed.

3.1 Comparison between FD-TD and Experiment in IR Band

Published results have shown good agreement between FD-TD and measurement in the GHz region [6]. To use FD-TD as a design tool, calculation is carried out to compare FD-TD and IR measurement results. The verification of the FD-TD

3D View of IR MDPC filter   Cross Section
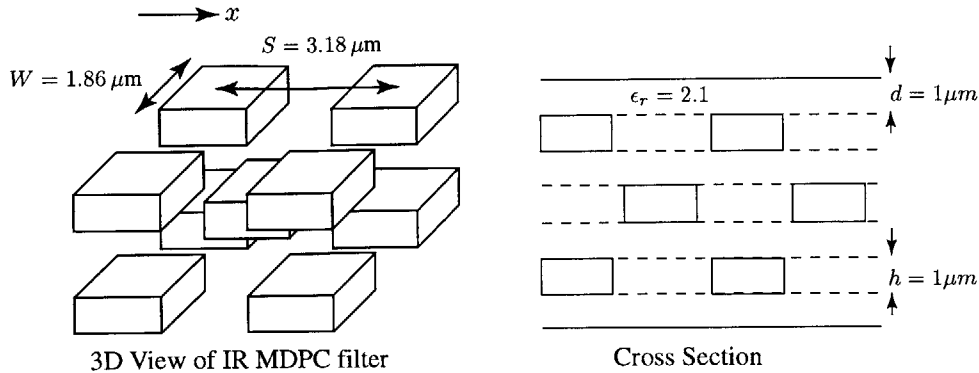
Figure 3-1: Geometry of the 3-D IR MDPC filter. Metallic parallelepipeds with square cross section is arranged in a face-center-cubic (100)-oriented crystal structure.

calculation for a 3D photonic crystal bandstop filter operating in the near infrared band is based on the published results in [4]. The geometry of the filter under study consists of metallic parallelepipeds with square cross section. These metal elements are embedded in a substrate of a planarizing polymer with a dielectric constant of $\epsilon_r = 2.1$. The elements are arranged such that they form the (100)-oriented face-centered cubic (fcc) crystal structure (Figure 3-1). The side of the square cross section is $1.86\,\mu$m, the center-to-center spacing is $3.18\,\mu$m and the thickness of the metal is $1\,\mu$m. The transmission of the filter was measured using a Fourier-transform spectrometer [4], with the effects of substrate and polymer compensated through a normalization measurement.

For the computer simulation, a normally incident field with a plane wave front and a Gaussian amplitude profile is used. The polarization of the incident electric field $\overline{E}_i$ is in the $\hat{x}$ direction. With FD-TD, the transmission coefficient of the $\hat{x}$ polarized wave is calculated. The transmission coefficients obtained are further attenuated by 5 dB to account for the experimental losses and the finite resistivity of the metal.

The comparison between the experimental measurement and FD-TD is shown in
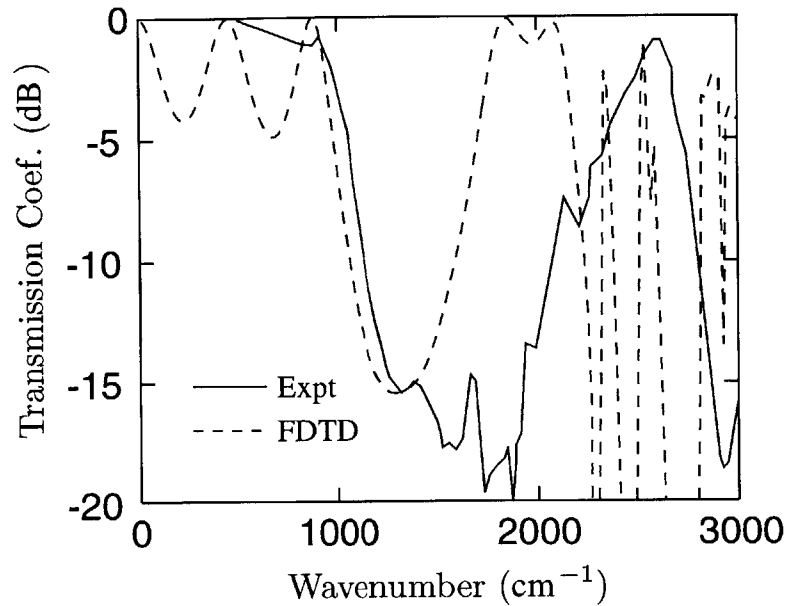
Figure 3-2: Comparison between FD-TD and experimental results of a 3D MDPC IR bandstop filter.

Figure 3-2. The solid line represents the experimental results and the dashed line shows the FD-TD results. Both display an onset of the stop band slightly below $1000\,\mathrm{cm}^{-1}$. However the calculated stop band has a smaller bandwidth and ends at approximately $1800\,\mathrm{cm}^{-1}$ instead of the measured $2500\,\mathrm{cm}^{-1}$. The difference between the two may be due to dispersion of the dielectric, metal losses and dielectric losses which are not accounted for by FD-TD. Also the discretization error from the gridding process of FD-TD may have caused the discrepancy. The small features of the experimental results are also due to potential incomplete normalization measurement of the polymer substrate. The comparison demonstrates that FD-TD is theoretically applicable to predict the electromagnetic behavior of photonic crystal filters in the IR spectrum and establishes the reliability of FD-TD as a design tool in the IR region.

3.2 Parametric Study at Normal Incidence

In order to analyze the dual stop bands of a MDPC structure, a parametric study is carried out. The geometry of the filter under study is based on the design in [6] and has three layers (Figure 3-3). Each layer consists of periodic metal patches embedded in the middle of a dielectric. It was found that with the metal at the middle of the dielectric of each layer, the performance of the filter improves, as the top half layer of the dielectric acts as a superstrate. The whole structure consists of three such layers, which are aligned along the z-axis. The metal is assumed to be perfectly conducting and the dielectric constant of the substrate for the parametric study is 2.3.
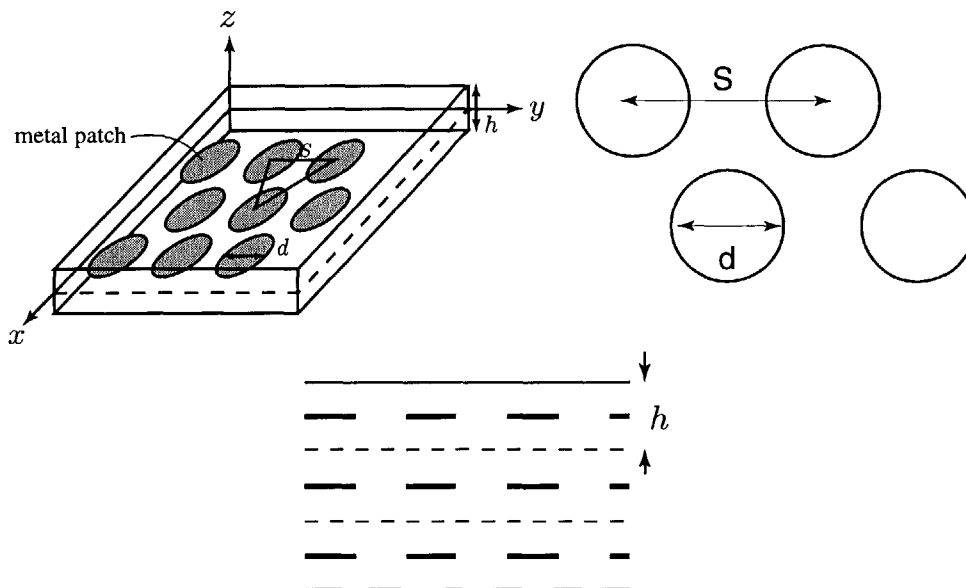
Figure 3-3: Geometry of the design of one layer used in the parametric study and final design. Circular metal discs are arranged in a triangular grid, and are embedded in a dielectric substrate of $\epsilon_r = 2.1$, 2.3.

A $\hat{y}$-directed TE pulse with a Gaussian amplitude profile and modulated by a

cosine function centered at $4000\,\text{cm}^{-1}$ is used as the incident wave. Circular patches are discretized into 40 Δ-steps across the diameter to minimize the discretization error [11]. The spacing between the centers of the circular patches is kept at $2\,\mu\text{m}$ throughout the four series, and the diameter of the patches is varied from $1\,\mu\text{m}$ to $1.58\,\mu\text{m}$ which corresponds to different percentage filling of metal from $25-60\,\%$ in a unit cell in each series.

The results from the normal incidence simulation are shown in Figure 3-5 to 3-8. The y-axes of the graphs show the transmission coefficients in dB and the x-axes show the wave number in $k = \frac{1}{\lambda_o}$, (cm^{-1}).
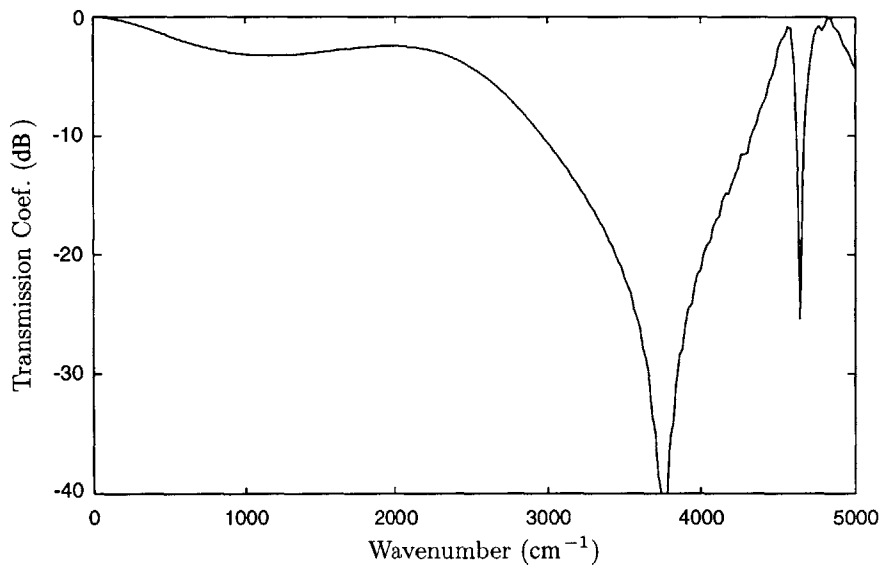
Figure 3-4: Transmission coefficients of bandstop filter with one layer of metal screen. $S = 2\,\mu\text{m}$, $d = 1.58\,\mu\text{m}$.

Figure 3-4 shows the transmission of one layer and only one major stop band is seen, which correlates with the separation between the elements. From Series A to D, the separation between the layers increases from $0.72\,\mu$m to $1.44\,\mu$m in four steps. In Figure 3-6 to 3-8, dual stop bands are observed. Although the structure is complicated, the formation of the stop bands can be explained. Two types of resonances are important in the formation of the stop bands. One is the resonance along the propagation direction, another one is the periodicity of the elements within the same layer.

Periodicity on the periodic surfaces contributes to the second stop band and the center frequency is determined by both the diameter of the circular patches and the spacing between the patches. The lattice constant, or the center to center separation S, determines the frequency at which the higher-order mode will start propagating. As the higher-order modes start propagating, the energy is diverted and creates a stop band in the fundamental mode. The patch itself acts as a reflector and as the filling percentage increases from 25% to 60%, the bandwidth of the second stop band can increase to over 50%.

The first stop band, on the other hand, only becomes apparent in the multilayer configuration and is not prominent for the case of one layer (Figure 3-4). The vertical resonance can be represented by a quarter-wave stack, because the metallic layer and the dielectric layer act as stack with alternating refractive indices. Since the metallic layer is not entirely filled (60 % maximum), the analogy is not complete. Nonetheless, there is a strong correlation between the two. Tabulated results (Table 3.1) show the shift of the resonance towards lower frequencies as the size of the patches increase.

$$k_{eff} = \frac{1}{4h\sqrt{\epsilon_r}}$$

As the inter-layer spacing further decreases, the dual stop bands merge to form
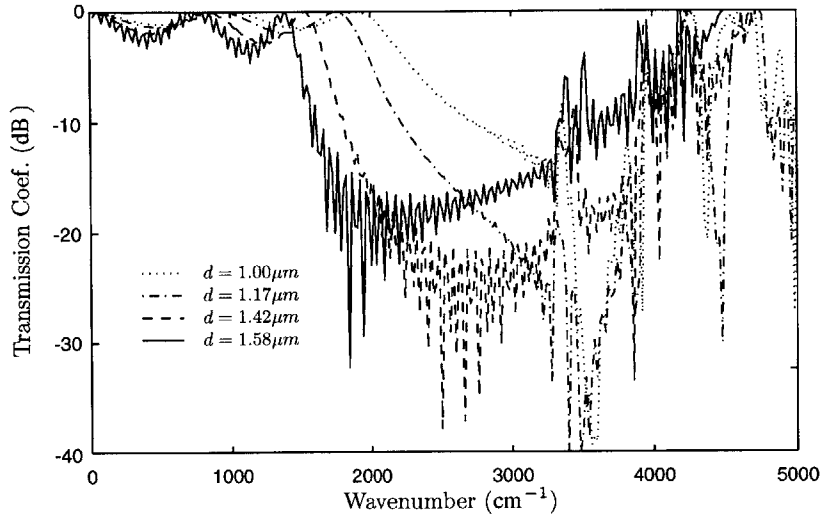
Figure 3-5: Series A. Transmission coefficients of bandstop filters with three aligned layers of metallic screens. $S = 2\,\mu\mathrm{m}$, $h = 0.72\,\mu\mathrm{m}$.
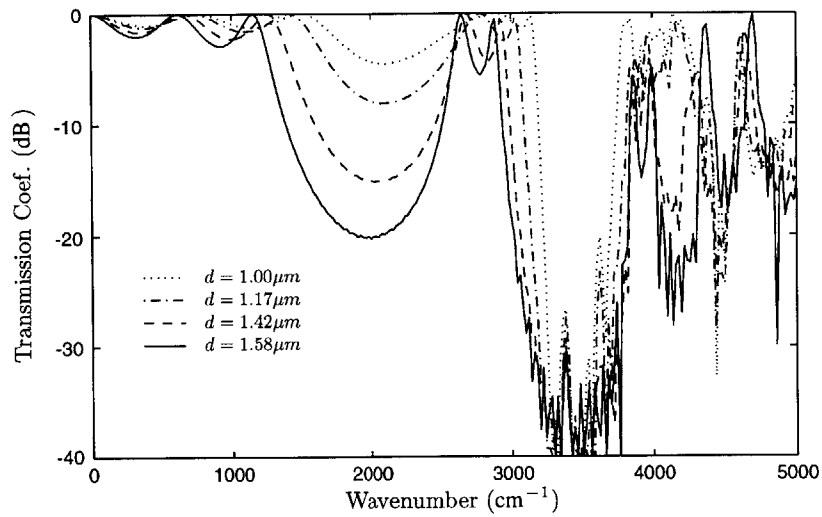
Figure 3-6: Series B. Transmission coefficients of bandstop filters with three aligned layers of metallic screens. $S = 2\,\mu\mathrm{m}$, $h = 0.96\,\mu\mathrm{m}$.
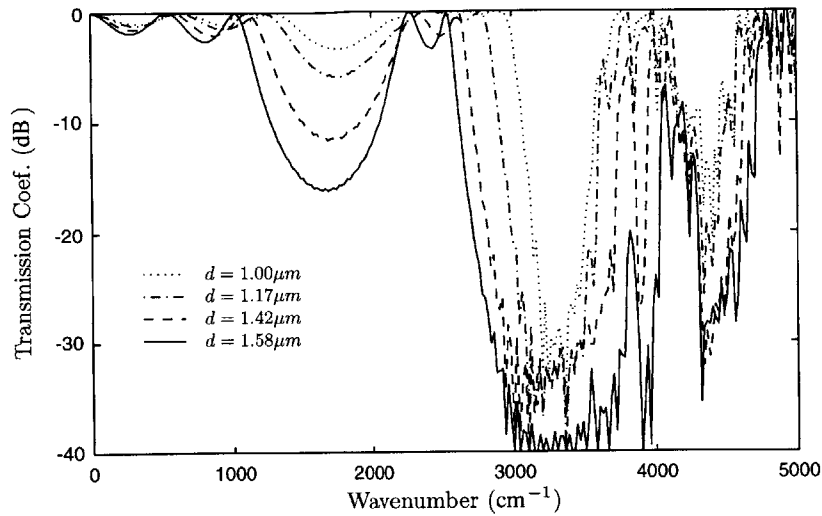
Figure 3-7: Series C. Transmission coefficients of bandstop filters with three aligned layers of metallic screens. $S = 2\,\mu$m, $h = 1.14\,\mu$m.
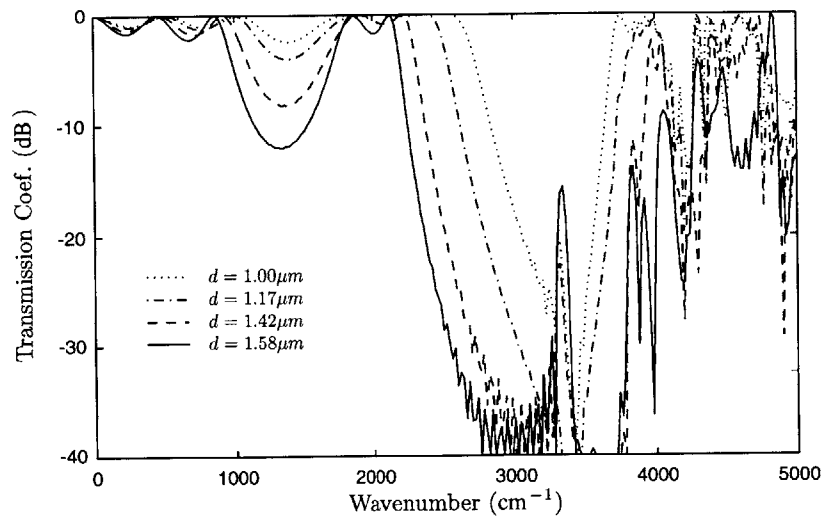
Figure 3-8: Series D. Transmission coefficients of bandstop filters with three aligned layers of metallic screens. $S = 2\,\mu$m, $h = 1.44\,\mu$m.

h	k_{eff}(calculated)
$0.72\,\mu$m	$2289\,\text{cm}^{-1}$
$0.96\,\mu$m	$1717\,\text{cm}^{-1}$
$1.14\,\mu$m	$1479\,\text{cm}^{-1}$
$1.44\,\mu$m	$1441\,\text{cm}^{-1}$

Table 3.1: Resonance frequency based on calculation.

an ultra wide stop band with a percentage bandwidth in excess of 70%.

To show the performance quantitatively, the relative bandwidth of each of the stop bands and the minima of the transmission coefficients are tabulated in Table 3.2.

Series	$\nu_{1c}(\text{cm}^{-1})$	$\frac{\Delta\nu_1}{\nu_1}$	$T_{1,min}(\text{dB})$	$\nu_{2c}(\text{cm}^{-1})$	$\frac{\Delta\nu_2}{\nu_2}$	$T_{2,min}(\text{dB})$
A, d=1.00 μm	N.A.	N.A.	N.A.	3330	0.37	−39
A, d=1.17 μm	N.A.	N.A.	N.A.	3070	0.56	−56
A, d=1.42 μm	N.A.	N.A.	N.A.	2850	0.74	−38
A, d=1.58 μm	N.A.	N.A.	N.A.	2460	0.70	−32
B, d=1.00 μm	N.A.	N.A.	−5	3460	0.16	−48
B, d=1.17 μm	N.A.	N.A.	−8	3450	0.21	−51
B, d=1.42 μm	2030	0.42	−15	3420	0.25	−49
B, d=1.58 μm	1950	0.57	−20	3390	0.27	−46
C, d=1.00 μm	N.A.	N.A.	−3	3320	0.15	−34
C, d=1.17 μm	N.A.	N.A.	−6	3250	0.21	−43
C, d=1.42 μm	1710	0.23	−12	3230	0.32	−42
C, d=1.58 μm	1660	0.47	−17	3340	0.42	−50
D, d=1.00 μm	N.A.	N.A.	−2	3240	0.25	−42
D, d=1.17 μm	N.A.	N.A.	−4	3170	0.35	−50
D, d=1.42 μm	N.A.	N.A.	−8	3150	0.49	−53
D, d=1.58 μm	1330	0.29	−12	3140	0.57	−60

Table 3.2: Relative bandwidth and minimum transmission coefficients of the bandstop filters (parametric study).

3.3 Effects of Metal Thickness and Dielectric Constant of Substrate

3.3.1 Metal with Finite Thickness

Instead of the 3D element shown in Figure 3-1, the new IR filter features thin metal patches instead. With thin metal, the choice of dielectric substrate is wider as the substrate will not be confined to a planarizing one. This is because the deposition of a thinner metal layer results in a smoother surface. As shown later in this section, the permittivities of the dielectric substrate has a direct effect on the angular dispersion properties of the filter. The simulated structure consists of periodic square patches in a square grid. The sides of the patches are of length 3 cm and the sides of the grids are 6 cm. A metal patch with no thickness is simulated with only $\overline{E}_x$ and $\overline{E}_y$ to model the patch. A patch with finite thickness is modeled here by having an aspect ratio between thickness and width of $1 : 10$ and contains the value of $\overline{E}_z$ as well. The result is shown in Figure 3-9.

The changes in bandwidth and the position of resonance are very small between the two. Thus the calculation of the designs are based on infinitely thin metal patches.

3.3.2 Dielectric with High Permittivity

As the filter is required to perform its function over a wide range of angles the angular performance is very important. An analysis has been carried out regarding the choice of the dielectric constant of the substrate and superstrate and the trade off between high and low dielectric constant is discussed. Figure 3-10 shows an incident plane wave at $\theta_i = 45°$ and the output angles for dielectrics with different permittivity are $\theta_{t1} = 18.8°$ and $\theta_{t2} = 29°$. It is seen that as the dielectric constant increases, the filter
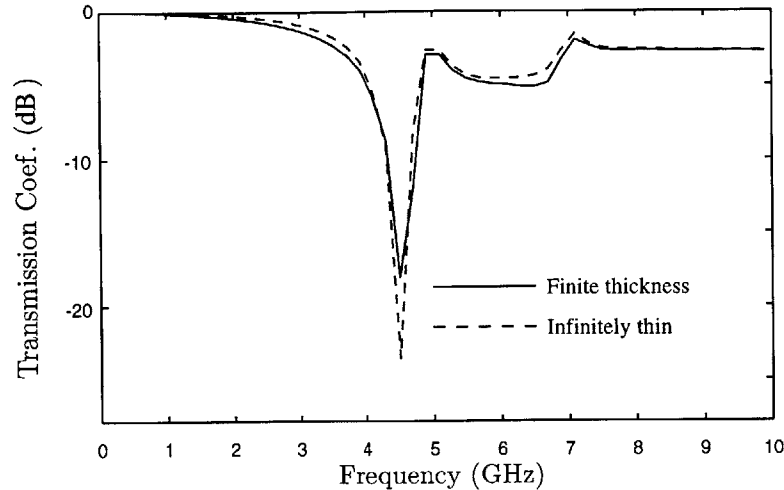
Figure 3-9: Infinitely thin metal vs. metal with finite thickness.

will be subjected to less angular dispersion. Oblique incidence calculations are carried out for the previous structure. The dielectric constants for comparison are chosen to be 2.3 and 4.8. Figure 3-11 and Figure 3-12 show the distortion of the shape of the stop band as the angle of incidence increase. While a higher index preserves the stop band characteristics over a wider range of angles, it also makes the fabrication of the MDPC more difficult. Higher dielectric constants also introduce higher out-of-band losses.

3.4 Optimal Design of Filter and Performance at Oblique Incidence

This section presents the final design of the IR filters which have a substrate with a dielectric constant of 2.1. The spacing between the elements is $3.2\,\mu$m, the separation
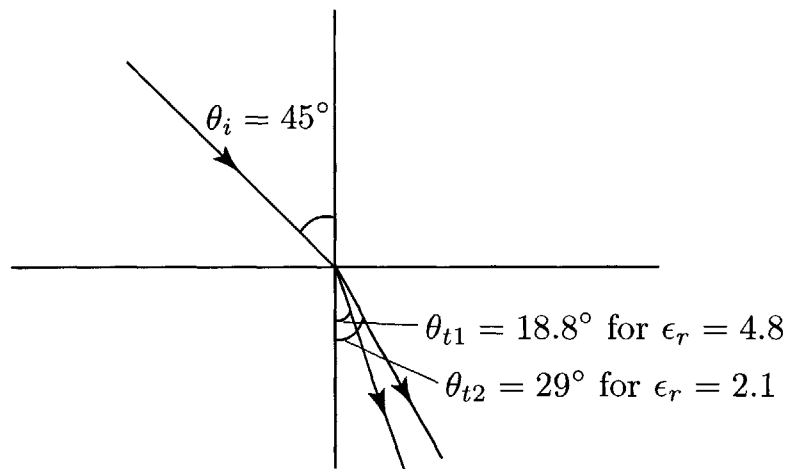
Figure 3-10: Internal angles for superstrates with different permittivities.

between the layers is $2.7\,\mu$m and the diameter of the disk is $2.6\,\mu$m.

$$
\begin{aligned}
\epsilon_r &= 2.1 \\
S &= 3.2\,\mu\text{m} \\
h &= 2.7\,\mu\text{m} \\
d &= 2.6\,\mu\text{m}
\end{aligned}
$$

Two implementations are analyzed, one of them uses aligned metal patches and the other one uses a face-center-cubic structure. The structures have a six-fold symmetry along the azimuthal direction. The azimuthal angles $\phi = 0°$ and $\phi = 90°$ represent the best and worst cases as the azimuthal angles varies and the transmission coefficients at different polar angles are calculated for different polarization (TE and TM). It is found that the alignment of the thin metallic patches does not change the properties of the stop bands very much.
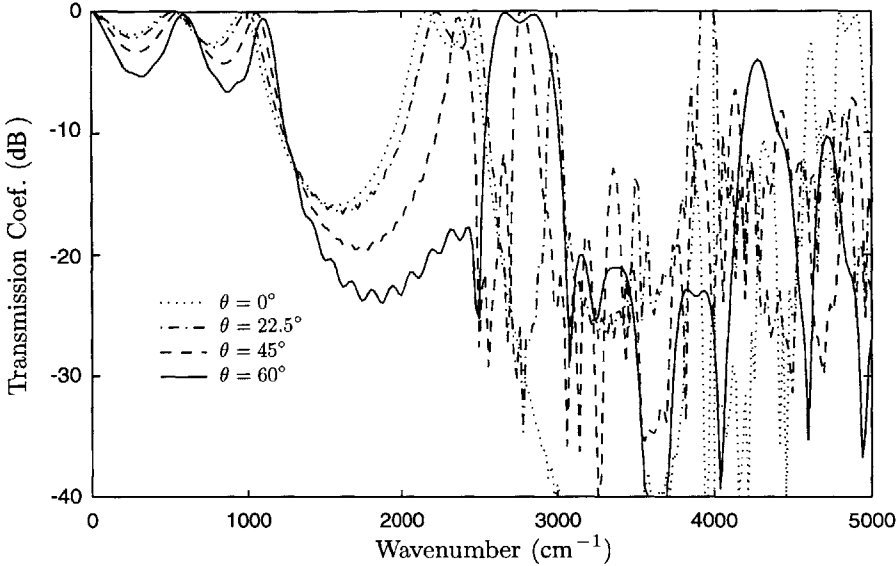
Figure 3-11: Transmission characteristics with substrate having $\epsilon_r = 2.3$.
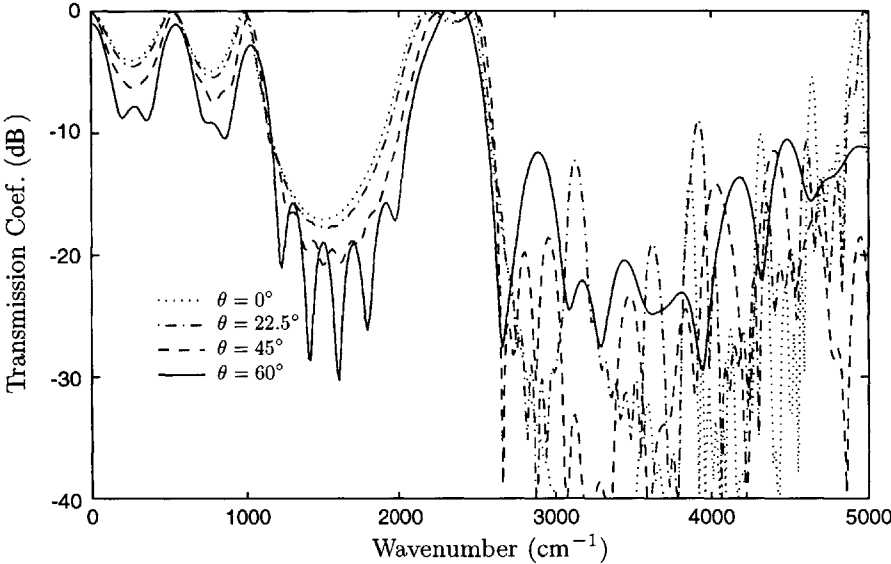
Figure 3-12: Transmission characteristics with substrate having $\epsilon_r = 4.8$.

3.4.1   Aligned Structure

Figure 3-14 and Figure 3-15 show the transmission characteristics of the filter upon TE and TM incidence with azimuthal angle $\phi = 0°$. We can see that the dual stop band for the TE incidence persists from $0°$ to $60°$. The upper edge of the low frequency band is more susceptible to the angular dispersion, and it shifts up the spectrum as the polar angle increases. This can be due to the low dielectric constant of the substrate and also the blue shift because of the vertically aligned stack, analogous to a dielectric mirror. For the second band, there is a same tendency for the upper edge to shift up the spectrum. For TM incidence, there is a significant degradation of performance for
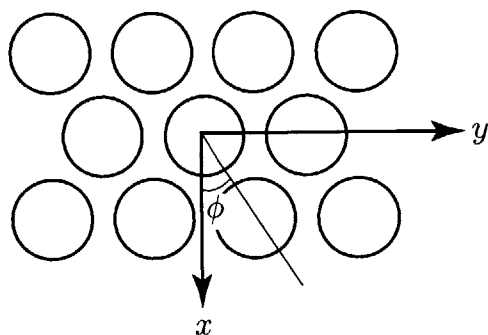
Figure 3-13: Azimuthal angle of incidence ϕ with respect to the filter.

the second band. This might be due to the thin metallic elements which are incapable of scattering the incident EM wave with the polarization perpendicular to the metal at large polar angles. For the first resonance, both the lower edge and upper edge of the band experience a blue shift as the incident angle goes higher. The quantitative performance of the filter is presented in Table 3.3, which show the relative bandwidth and the minima of the transmission spectrum.

Figure 3-16 and Figure 3-17 show the results of the transmission characteristics of the filter upon TE and TM incidence with azimuthal angle $\phi = 90°$. The first stop

band, for both TE and TM exhibit similar characteristics as when the azimuthal angle of incidence is $\phi = 0°$. The second stop band has different characteristics because of the azimuthal asymmetry. Consequently, the stop band is only partial and subjected to variation upon changing the polar angle of incidence.

In conclusion, for the aligned structure, with TE incidence, the stop band transmission is below $-10\,\mathrm{dB}$ for $8 - 12\,\mu\mathrm{m}$ and the stop band at higher frequencies has a partial stop band from $3 - 5\,\mu\mathrm{m}$.
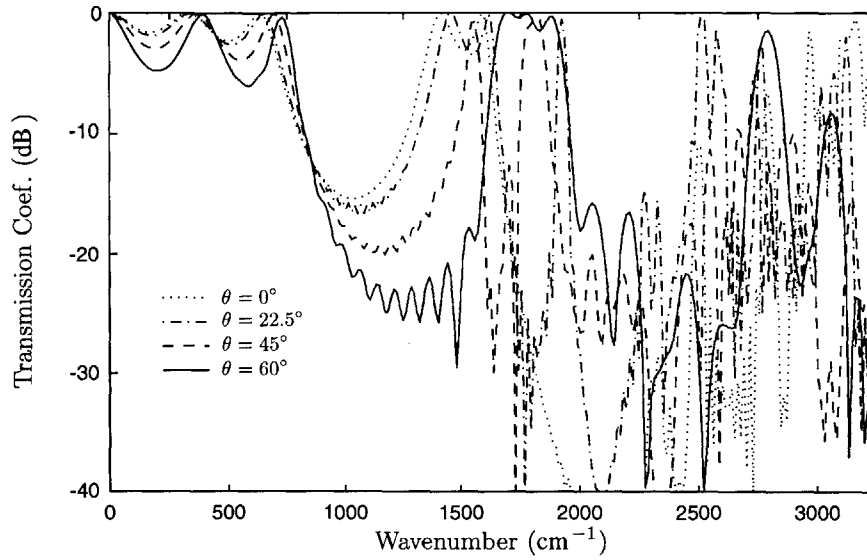
Figure 3-14: Transmission coefficient for TE incidence, $\theta = 0° - 60°$, $\phi = 0°$.
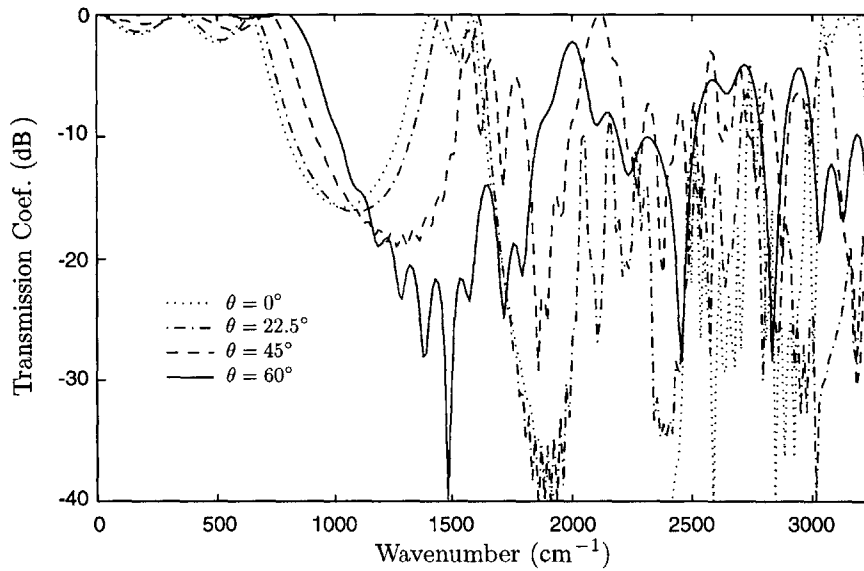
Figure 3-15: Transmission coefficient for TM incidence, $\theta = 0° - 60°$, $\phi = 0°$.
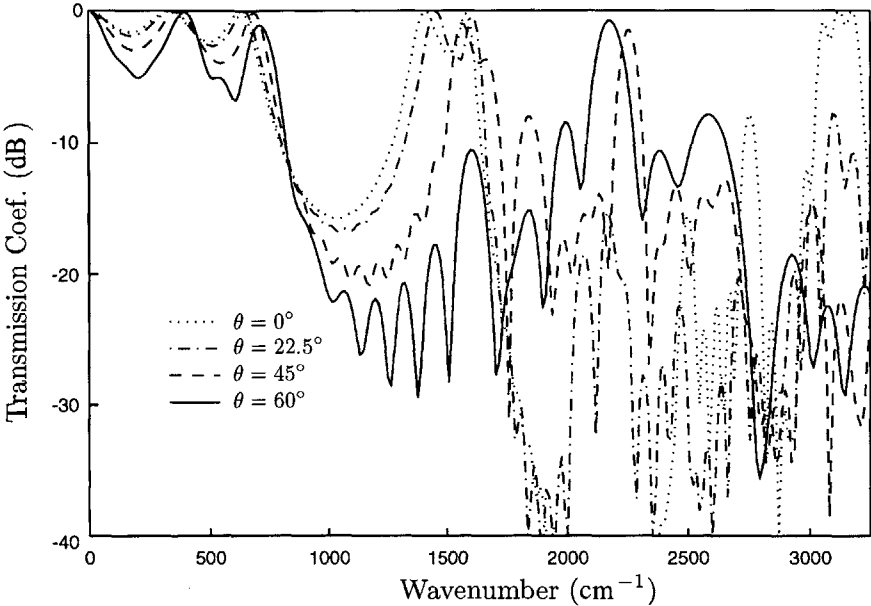
Figure 3-16: Transmission coefficient for TE incidence, $\theta = 0° - 60°$, $\phi = 90°$.

Figure 3-17: Transmission coefficient for TM incidence, $\theta = 0° - 60°$, $\phi = 90°$.

Series		$\nu_{1c}(\text{cm}^{-1})$	$\frac{\Delta\nu_1}{\nu_1}$	$T_{1,min}(\text{dB})$	$\nu_{2c}(\text{cm}^{-1})$	$\frac{\Delta\nu_2}{\nu_2}$	$T_{2,min}(\text{dB})$
TE $\theta = 0°$	$\phi = 0°$	1035	0.45	-15	2210	0.51	-52
TE $\theta = 22.5°$	$\phi = 0°$	1065	0.48	-16	2215	0.24	-44
TE $\theta = 45°$	$\phi = 0°$	1150	0.57	-20	2320	0.29	-46
TE $\theta = 60°$	$\phi = 0°$	1035	0.75	-25	2340	0.32	-42
TM $\theta = 0°$	$\phi = 0°$	1030	0.47	-16	2185	0.50	-70
TM $\theta = 22.5°$	$\phi = 0°$	1080	0.46	-16	2155	0.50	-45
TM $\theta = 45°$	$\phi = 0°$	1220	0.49	-19	N.A.	N.A.	N.A.
TM $\theta = 60°$	$\phi = 0°$	1430	0.60	-25	N.A.	N.A.	N.A.
TE $\theta = 0°$	$\phi = 90°$	1035	0.45	-16	2180	0.49	-60
TE $\theta = 22.5°$	$\phi = 90°$	1060	0.49	-17	2365	0.60	-46
TE $\theta = 45°$	$\phi = 90°$	1150	0.57	-20	2025	0.17	-33
TE $\theta = 60°$	$\phi = 90°$	1200	0.67	-20	N.A.	N.A.	N.A.
TM $\theta = 0°$	$\phi = 90°$	1025	0.44	-15	2225	0.52	-55
TM $\theta = 22.5°$	$\phi = 90°$	1080	0.44	-15	1975	0.35	-37
TM $\theta = 45°$	$\phi = 90°$	1225	0.45	-15	N.A.	N.A.	N.A.
TM $\theta = 60°$	$\phi = 90°$	1275	0.43	-25	N.A.	N.A.	N.A.

Table 3.3: Relative bandwidths of the dual stop bands at different incident angles (aligned structure).

3.4.2 Face-Center-Cubic Structures
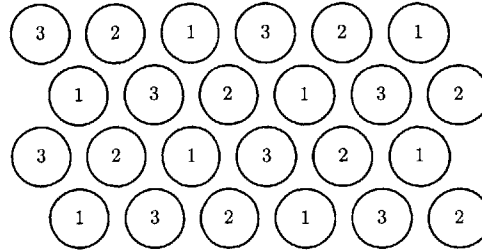
Figure 3-18: Relative position of the metal patches at different layers for a face-center-cubic structure.

In this section a second implementation of the filter is presented. In the aligned design, the metal patches are stacked on top of each other, hence the performance for different azimuthal and polar angle of incidence may degrade as the cross section of metal as seen by the incident wave decreases.

For the face-center-cubic (fcc) case, the metal patches are arranged such that between each layer there is an offset. The vertical period comprises three layers 1, 2 and 3. The relative position of the labeled metal patches is shown in Figure 3-18, which indicate the center position of the patches. This configuration is expected to have a more consistent performance for different azimuthal angles of incidence. The unit cells used are shown in Figure 3-19.

For TE incident with $\phi = 0°$, the pass band up to $12\,\mu$m has a transmission
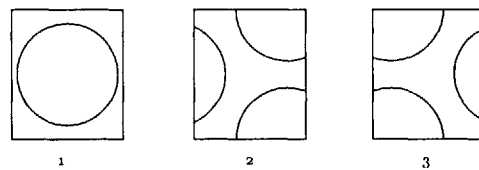
Figure 3-19: Unit cell for face-center-cubic structure.

coefficient of less than -3 dB in the case of normal incidence and the stop band from $8 - 12 \, \mu$m has a transmission coefficient of less than -15 dB. Due to the offset between layers, the lower edge of the second stop band is not as steep as the aligned one.

For TM incidence with $\phi = 0°$, no significant improvement is observed. Similar to the aligned case, the second stop band degrades very fast and the transmission coefficient starts oscillating above the -10 dB level as the polar angle is off normal. Both TE and TM at $\phi = 90°$ incidence show an improvement over the aligned structure. The second stop band appears to be more stable over a wider range of polar angles. Overall, the face-center-cubic structure offers slightly more consistent transmission characteristics along the azimuthal direction.

For comparison, the center frequencies, relative bandwidth, minimum transmission coefficient in (dB) for the face-center-cubic implementations are tabulated in Table 3.4.
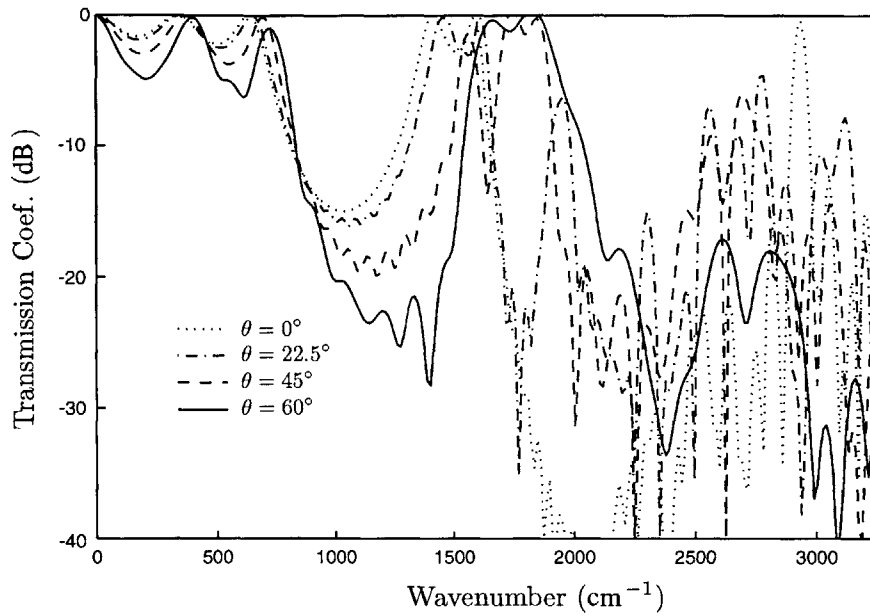
Figure 3-20: Transmission coefficient (fcc) for TE incidence, $\theta = 0° - 60°$, $\phi = 0°$.
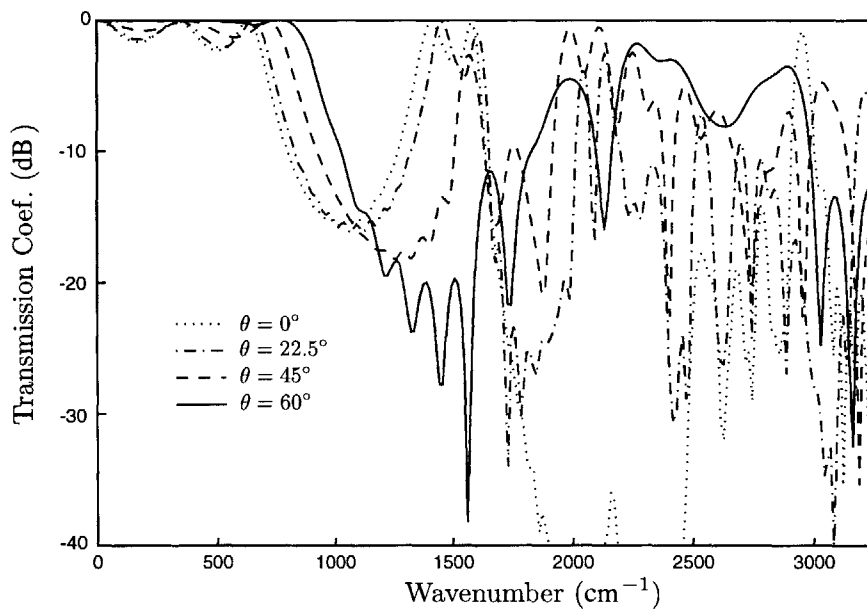
Figure 3-21: Transmission coefficient (fcc) for TM incidence, $\theta = 0° - 60°$, $\phi = 0°$.

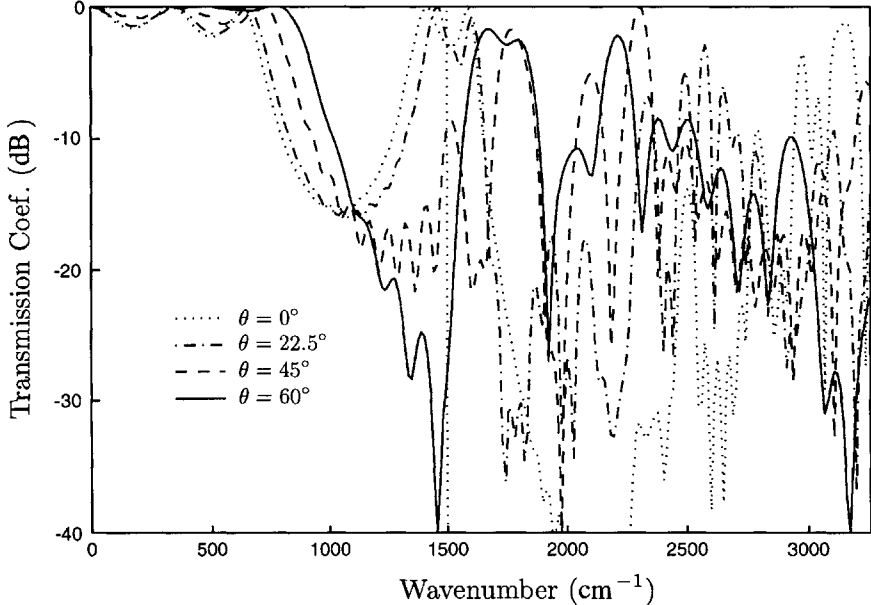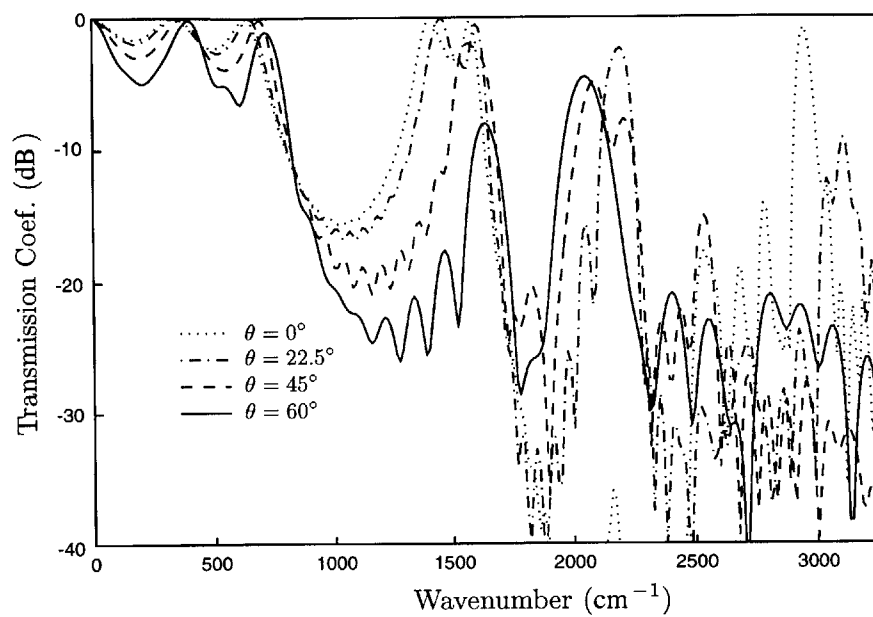Figure 3-22: Transmission coefficient (fcc) for TE incidence, $\theta = 0° - 60°$, $\phi = 90°$.
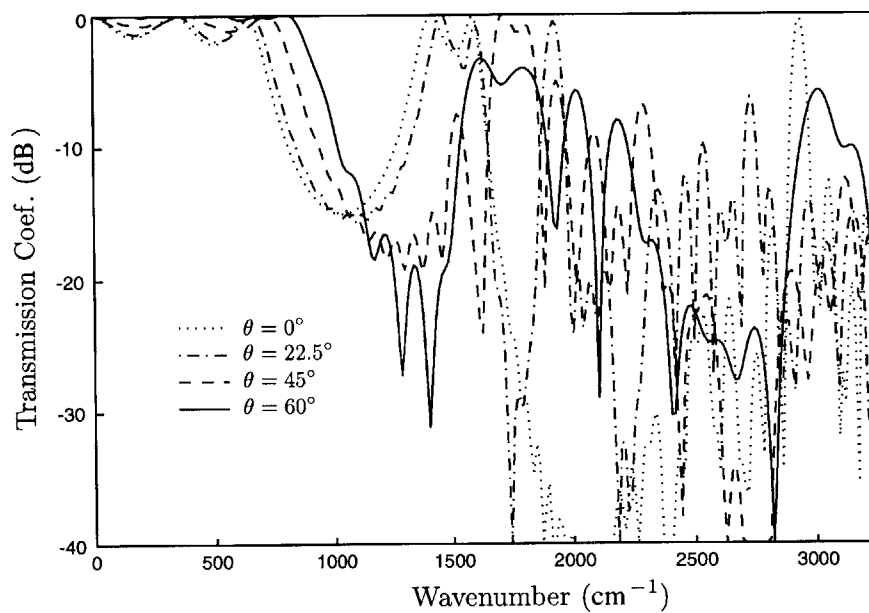
Figure 3-23: Transmission coefficient (fcc) for TM incidence, $\theta = 0° - 60°$, $\phi = 90°$.

Series		$\nu_{1c}(\text{cm}^{-1})$	$\frac{\Delta\nu_1}{\nu_1}$	$T_{1,min}(\text{dB})$	$\nu_{2c}(\text{cm}^{-1})$	$\frac{\Delta\nu_2}{\nu_2}$	$T_{2,min}(\text{dB})$
TE $\theta = 0°$	$\phi = 0°$	1040	0.46	-15	2275	0.55	-52
TE $\theta = 22.5°$	$\phi = 0°$	1070	0.47	-16	2275	0.24	-40
TE $\theta = 45°$	$\phi = 0°$	1170	0.56	-18	2220	0.29	-44
TE $\theta = 60°$	$\phi = 0°$	1170	0.60	-22	2520	0.38	-33
TM $\theta = 0°$	$\phi = 0°$	1040	0.46	-15	2275	0.55	-67
TM $\theta = 22.5°$	$\phi = 0°$	1070	0.47	-15	2350	0.13	-35
TM $\theta = 45°$	$\phi = 0°$	1215	0.47	-18	N.A.	N.A.	N.A.
TM $\theta = 60°$	$\phi = 0°$	1430	0.56	-20	N.A.	N.A.	N.A.
TE $\theta = 0°$	$\phi = 90°$	1040	0.46	-15	2275	0.55	-67
TE $\theta = 22.5°$	$\phi = 90°$	1065	0.50	-16	2675	0.32	-48
TE $\theta = 45°$	$\phi = 90°$	1160	0.62	-18	2875	0.43	-37
TE $\theta = 60°$	$\phi = 90°$	1200	0.67	-22	2825	0.48	-33
TM $\theta = 0°$	$\phi = 90°$	1040	0.46	-15	2275	0.55	-52
TM $\theta = 22.5°$	$\phi = 90°$	1085	0.43	-15	2340	0.31	-42
TM $\theta = 45°$	$\phi = 90°$	1225	0.45	-17	2900	0.40	-48
TM $\theta = 60°$	$\phi = 90°$	1270	0.39	-20	2580	0.28	-44

Table 3.4: Relative bandwidths of the dual stop bands at different incidence angles (fcc structure).

Chapter 4

Hybrid Method for Multilayer Analysis

In this chapter, the formulation of a hybrid method for treating multilayer structures is presented. The transfer matrix method is used in conjunction with the FD-TD calculation.

The transfer matrix method has been applied to many circuit and transmission line problems. Application to the cascade of metallic periodic screens has been discussed in [17, 18, 19]. In [20], computation of the scattered fields from free-standing metal patches was computed by frequency domain methods, combined with the matrix formulation given in [17], where the cascade of a metal screen with different dielectric slabs was analyzed. Cascading of grating screens and formulation for shifted units was presented by Hall [18]. The generalized scattering matrix [19] takes into account higher-order modes and evanescent coupling between closely spaced layers. Cascading of multiple metal screens with dielectric slabs was also analyzed.

The elements of the scattering matrix consist of the forward scattering and the backward scattering coefficients of different modes and are usually calculated by

means of frequency domain method [21], such as the Method of Moments. Since these methods are frequency domain methods, they can only calculate the scattering coefficients for one frequency at a time. Also, careful selection of basis functions is needed for complicated geometries. The FD-TD technique allows the calculation of the scattering coefficients over a wide frequency spectrum with one simulation and can handle complicated multilayer geometries. With the hybrid method, which combines FD-TD with the transfer matrix method, multi-layer results can be synthesized from the scattering coefficients of a single layer. Dielectric substrates and layer thickness can also be varied without running a full EM simulation.

4.1   Generalized Scattering Matrix

The generalized scattering matrix describes the scattering properties of a single filter layer. In general, a multilayer filter has layers of metal screens and dielectric slabs of various permittivities ϵ_n and thicknesses d_n (Figure 4-1). The problem can be separated into a "metallic part" and "dielectric part". For the metallic part, FD-TD is used. For the dielectric parts, analytic coefficients can be used, as described later in this chapter. The results are then combined by using the transfer matrix method.

To obtain the scattering coefficients from a FD-TD simulation, we can consider a field incident on the metal screen with wavevector $\overline{k}_i$ defined according to Figure 4-2. $\overline{E}_i$ and $\overline{k}_i$ can be expressed as:

$$\overline{E}_i = \overline{E}_o e^{i\overline{k}_i \cdot \overline{r}}$$
$$\overline{k}_i = k_{ix}\hat{x} + k_{iy}\hat{y} + k_{iz}\hat{z} \tag{4.1}$$

Based on Fourier transform of the time domain scattered electric field, the scattered
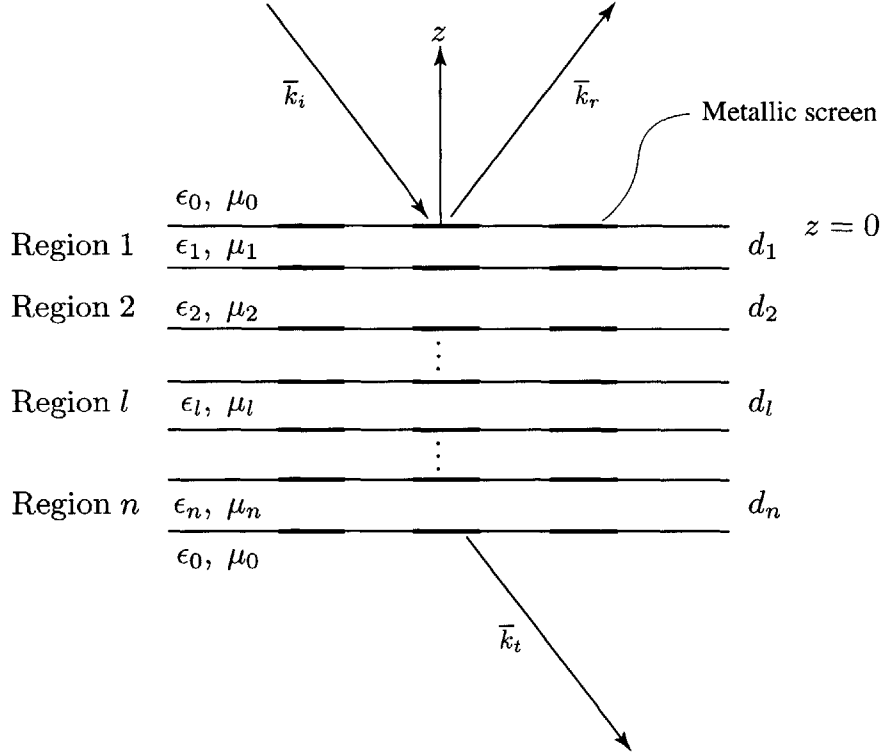
Figure 4-1: General structure of a multilayer filter.

field in the frequency domain can be found. The scattered fields, however, cannot be represented by a single k-vector, because the periodic surface creates a grating effect in both $\hat{x}$ and $\hat{y}$ direction when the frequency is high enough. Mathematically, the scattered field $\overline{E}_s$ can be represented as a summation over the spatial harmonics the Floquet modes,

$$\overline{E}_s = \sum_{m=-\infty}^{\infty} \sum_{n=-\infty}^{\infty} \overline{E}_s^{mn} e^{i\overline{k}_s \cdot \overline{r}} \tag{4.2}$$

where $\overline{k}_s$ is the wavevector of the scattered wave. By phase matching on the periodic
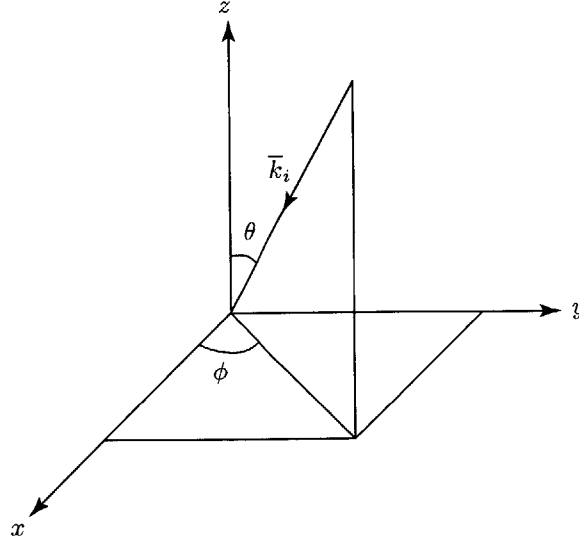
Figure 4-2: Orientation of incident wavevector $\overline{k}_i$.

surface, the wavevectors $\overline{k}_s^{mn}$ can be written in component form as:

$$\overline{k}_s^{mn} = \left(k_{ix} + \frac{2m\pi}{p_x} \right) \hat{x} + \left(k_{iy} + \frac{2n\pi}{p_y} \right) \hat{y} + k_z^{mn} \hat{z} \qquad (4.3)$$

where m and n are integers and describe the spatial modes and

$$k_z^{mn} = \sqrt{k^2 - k_{sx(mn)}^2 + k_{sy(mn)}^2} \qquad (4.4)$$

with $k = \omega \sqrt{\mu \epsilon_s}$ describing the dispersion relation in the scattered medium. Each $\overline{k}_s^{mn}$ can be interpreted as a plane wave travelling at a particular direction governed by the phase matching condition. The direction and hence the corresponding polar angle θ and azimuthal angle ϕ are frequency dependent. To obtain the scattering coefficient for each individual mode, we can integrate the scattered fields times the conjugates

of different spatial harmonics on the observation plane in the FD-TD computation domain.

$$E_s^{mn} = \frac{1}{S} \int_{p_x} \int_{p_y} dx dy E_s e^{-ik_x^{mn}x} e^{-ik_y^{mn}y} \tag{4.5}$$
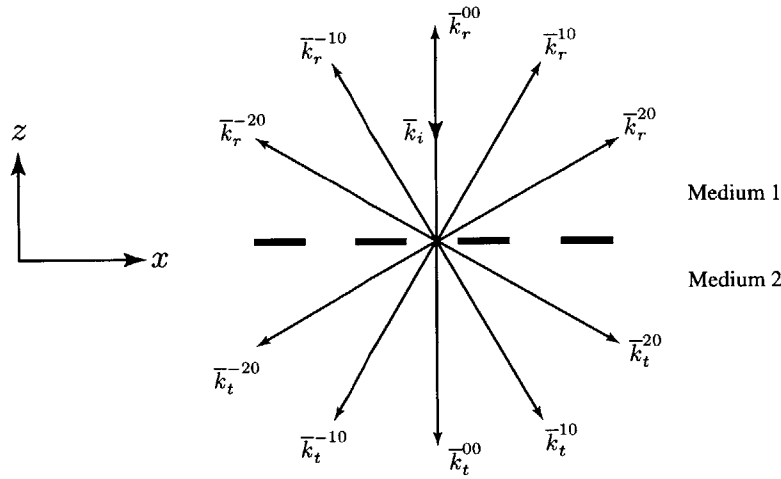
Figure 4-3: Scattering of different modes from a periodic surface.

The scattering process can be represented graphically as shown in Figure 4-3, where the normally incident wavevector is $\bar{k}_i$, the reflected wavevectors are $\bar{k}_r^{mn}$ and the transmitted wavevectors $\bar{k}_t^{mn}$. Here, m and n denote the index of the mode. Only the wavevectors on the $x - z$ plane are shown here ($n = 0$).

A generalized scattering matrix takes into account the interactions between all the modes of the unit layer. But in practice the matrix can represent only a truncated sum of modes. Depending on the geometry, the incident wave polarization, the incidence angle and the proximity between successive layers, a rule for determining the number of modes included can be set. For normal incidence with elements that are insensitive to polarization, such as circular patches, a circle in the $k_x - k_y$ plane can be used to

select the number of modes to be computed. Modes with indices m, n that are within the boundary of the circle can be included into the generalized scattering matrix (Figure 4-4). For example, in the case of normal incidence we can set the radius to be u1nity when the periodic surfaces are far apart.
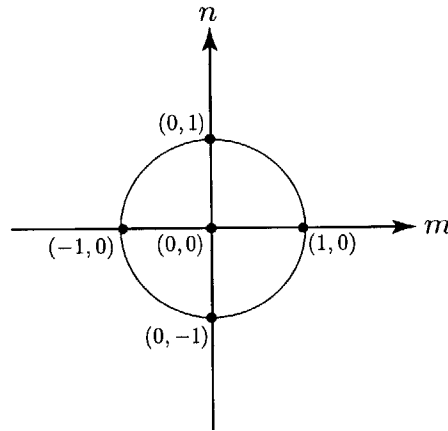
Figure 4-4: Truncated sum of modes. Modes are computed if they fall within a circle of finite radius.

For the interaction between the included modes, we can write down a generalized scattering matrix representing the scattering at each frequency of interest:

$$
\begin{bmatrix} \overline{E}_{1s} \\ \overline{E}_{2s} \end{bmatrix} = \begin{bmatrix} \overline{\overline{S}}_{11} & \overline{\overline{S}}_{12} \\ \overline{\overline{S}}_{21} & \overline{\overline{S}}_{22} \end{bmatrix} \cdot \begin{bmatrix} \overline{E}_{1i} \\ \overline{E}_{2i} \end{bmatrix} \tag{4.6}
$$

The generalized scattering matrix is similar to the S matrix of microwave networking, except that the elements of the matrix are themselves matrices and may represent cross-mode scattering. $\overline{\overline{S}}_{11}$ and $\overline{\overline{S}}_{22}$ are the complex backward scattering matrices and $\overline{\overline{S}}_{12}$ and $\overline{\overline{S}}_{21}$ are the complex forward scattering matrices. The dimension of the generalized scattering matrix depends on the number of modes included. The column matrix on the left-hand side represents the scattered fields and the column

Figure 4-5: Graphical representation of the scattering matrix.

matrix on the right-hand side represents the incident fields. In order to cascade the matrices, we have to put the field quantities from the same medium within the same column vector, and form the transfer matrix equation:

$$
\begin{bmatrix} \overline{E}_{2s} \\ \overline{E}_{2i} \end{bmatrix} = \begin{bmatrix} \overline{\overline{T}}_{11} & \overline{\overline{T}}_{12} \\ \overline{\overline{T}}_{21} & \overline{\overline{T}}_{22} \end{bmatrix} \cdot \begin{bmatrix} \overline{E}_{1i} \\ \overline{E}_{1s} \end{bmatrix}
\tag{4.7}
$$

The elements or submatrices can be calculated as follows:

$$
\begin{aligned}
\overline{\overline{T}}_{11} &= \left[\overline{\overline{S}}_{21} - \overline{\overline{S}}_{22} \cdot \overline{\overline{S}}_{12}^{-1} \cdot \overline{\overline{S}}_{11} \right] \\
\overline{\overline{T}}_{12} &= \overline{\overline{S}}_{22} \cdot \overline{\overline{S}}_{12}^{-1} \\
\overline{\overline{T}}_{21} &= -\overline{\overline{S}}_{12}^{-1} \cdot \overline{\overline{S}}_{11} \\
\overline{\overline{T}}_{22} &= \overline{\overline{S}}_{12}^{-1}
\end{aligned}
$$

$$
\tag{4.8}
$$

and the elements of $\overline{\overline{S}}$ are related back to $\overline{\overline{T}}$ by

$$
\begin{aligned}
\overline{\overline{S}}_{11} &= -\overline{\overline{T}}_{22}^{-1} \cdot \overline{\overline{T}}_{21} \\
\overline{\overline{S}}_{12} &= \overline{\overline{T}}_{22}^{-1} \\
\overline{\overline{S}}_{21} &= \left[\overline{\overline{T}}_{11} - \overline{\overline{T}}_{12} \cdot \overline{\overline{T}}_{22}^{-1} \cdot \overline{\overline{T}}_{21} \right]
\end{aligned}
$$

$$\overline{\overline{S}}_{22} \;=\; \overline{\overline{T}}_{12} \cdot \overline{\overline{T}}_{22}^{-1}$$

(4.9)

In matrix (4.7), the column matrix on the left-hand side represents the field quantities from medium 2 and the column matrix on the right-hand side represents the field quantities of medium 1. The vector notation implies that each column vector consists of the field quantities of the different modes.

The matrix $\overline{\overline{S}}$ is the generalized scattering matrix and consists of sub-matrices $\overline{\overline{S}}_{mnpq}$. The sub-matrix $\overline{\overline{S}}_{mnpq}$ on the diagonal represent scattering between the same mode and the off diagonal ones represent the cross-mode interaction. To investigate the properties of a particular sub-matrix, we can consider an interaction between a incident pq mode and the scattered mn mode. The superscript H represents a TE wave, while V represents a TM wave. The sub-matrices take into account of both co-polarization and cross-polarization. The sub-matrices of the scattering matrices are related to the field quantities by:

$$
\begin{bmatrix} \overline{E}_{1s}^{H(mn)} \\ \overline{E}_{2s}^{V(mn)} \end{bmatrix}
=
\begin{bmatrix} \overline{\overline{S}}_{mnpq}^{HH} & \overline{\overline{S}}_{mnpq}^{HV} \\ \overline{\overline{S}}_{mnpq}^{VH} & \overline{\overline{S}}_{mnpq}^{VV} \end{bmatrix}
\cdot
\begin{bmatrix} \overline{E}_{1i}^{H(pq)} \\ \overline{E}_{2i}^{V(pq)} \end{bmatrix}
$$

(4.10)

To relate the sub-matrices to the scattering coefficient from the scattering coefficients calculated by FD-TD, we can write $\overline{\overline{S}}_{mnpq}$ in terms of a scattering matrix. For the case of TE-TE scattering,

$$
\begin{bmatrix} E_{1s}^{H(mn)} \\ E_{2s}^{H(mn)} \end{bmatrix}
=
\begin{bmatrix} S_{11} & S_{12} \\ S_{21} & S_{22} \end{bmatrix}
\cdot
\begin{bmatrix} E_{1i}^{H(pq)} \\ E_{2i}^{H(pq)} \end{bmatrix}
$$

(4.11)

The elements are no longer matrices but complex scattering coefficients that are obtained from the FD-TD code.

4.2 Transfer Matrix for Dielectric

In the transfer matrix equation, $\overline{\overline{T}}$ may either be the transfer matrix of a metallic filter layer or a dielectric slab. For dielectric, the reflection and transmission coefficient can be analytically derived [16]. Consider the layered medium in Figure 4-1. The wave in each layer consists of an upgoing wave and a downgoing wave, at each interface, the tangential electric and magnetic field has to be continuous, and the matrix equation which governs the amplitudes of the waves is

$$
\begin{bmatrix} E_{2s}^{mn} \\ E_{2i}^{mn} \end{bmatrix} = \frac{1}{2}(1 + p_{21}) \begin{bmatrix} R_{21} & 1 \\ 1 & R_{21} \end{bmatrix} \begin{bmatrix} E_{1i}^{mn} \\ E_{1s}^{mn} \end{bmatrix} \tag{4.12}
$$

which accounts for the boundary between each different dielectric. In the above equation,

$$
p_{21}^{TE} = \frac{\epsilon_2 k_{1z}}{\epsilon_1 k_{2z}} \tag{4.13}
$$

for TE modes and

$$
p_{21}^{TM} = \frac{\mu_2 k_{1z}}{\mu_1 k_{2z}} \tag{4.14}
$$

for TM modes.

$$
R_{21} = \frac{1 - p_{21}}{1 + p_{21}} \tag{4.15}
$$

is the Fresnel reflection coefficient. Inside the dielectric, the propagation matrix is:

$$
\begin{bmatrix} E_{2s}^{mn} \\ E_{2i}^{mn} \end{bmatrix} = \begin{bmatrix} e^{-ik_2 d_2} & 0 \\ 0 & e^{ik_2 d_2} \end{bmatrix} \begin{bmatrix} E_{1i}^{mn} \\ E_{1s}^{mn} \end{bmatrix} \tag{4.16}
$$

With both the magnitude and the phase, the effects of the separation between the filters can be correctly calculated. The complex scattering coefficients from the FD-TD simulation and the analytic expressions permit a hybrid wide band matrix

method. The above formulation allows the cascade of multilayer filters with arbitrary incident plane wave and changes the scattering equation

$$\overline{E}_s = \overline{\overline{S}} \cdot \overline{E}_i \qquad (4.17)$$

to a transmission equation:

$$\overline{E}_2 = \overline{\overline{T}} \cdot \overline{E}_1 \qquad (4.18)$$

Thus for a multilayer structure,

$$\overline{E}_n = \overline{\overline{T}}_n \cdot \overline{\overline{T}}_{n,n-1} \cdots \overline{\overline{T}}_{l,l-1} \cdots \overline{\overline{T}}_{1,0} \cdot \overline{E}_0 \qquad (4.19)$$

However, there are some limitations of the matrix methods. First of all, it requires the same spatial periodicity for each layer to be cascaded. Also, the accuracy of the calculation depends on the amount of higher-order modes included. When only interactions of fundamental modes are involved, and the geometry is simple, approximation formulas can be used. But when interactions of higher-order modes are considered, or when the geometry of the metal screen is complicated, an accurate EM modeling is needed to obtain the scattering coefficients and the matrix method has to take into account the higher-order modes.

In the next chapter, the results based on the hybrid method are presented.

Chapter 5

Simulation Results Based on Hybrid Method

In this chapter, the results of calculations based on the hybrid method are presented. Transmission coefficients of cascaded metal screens for both normal and oblique incidence are computed by the hybrid method. One of the examples is a dichroic plate reported in the literature and the other example is a structure with periodic square patches. The hybrid method results are compared to the hybrid MoM and full FD-TD simulation.

5.1 Dichroic Plate

In [22], a dichroic plate for radioastronomical use is reported. The structure of the unit filter is shown in Figure 5-1. The specification of the filter is such that it can reflect the low frequencies and transmit the high frequencies with low loss. A sandwich design is used to allow a relatively flat pass band performance. The cross section of the filter is shown in Figure 5-2. In [22], the transfer matrix method is used in
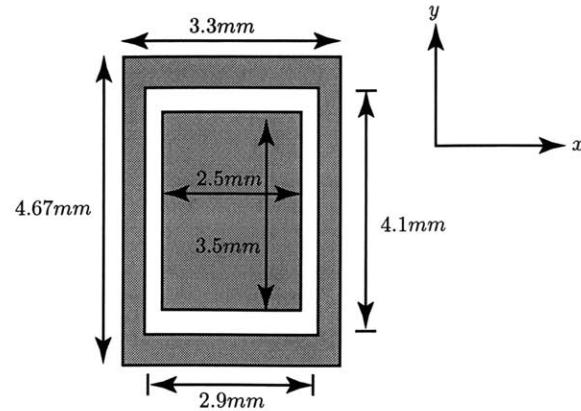
Figure 5-1: Geometry of the periodic surface used in the dichroic filter.

conjunction with Method of Moments. A hybrid approach described in Chapter 4 is used here to compare the results. The oblique FD-TD code is used to simulate the scattering of a single layer at 45° and the scattering coefficients are then used together with the transfer matrix. The comparison between the two is shown in Figure 5-4 and Figure 5-5. The horizontal axes represents the frequency in GHz and the vertical axes of the upper plots are the transmitted power normalized to 1. The lower plots show the phase of the transmitted plane wave. Both TE and TM incidence is used for a polar angle of 45° and azimuthal angle of 0°.
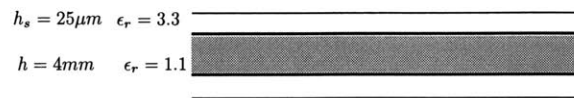

Figure 5-2: Cross section of the dichroic plate sandwich filter.

The results of the two methods show a good agreement. The magnitude and the phase for both polarizations correspond well to each other. The discrepancy may be due to the finite resolution of the discretization processes.
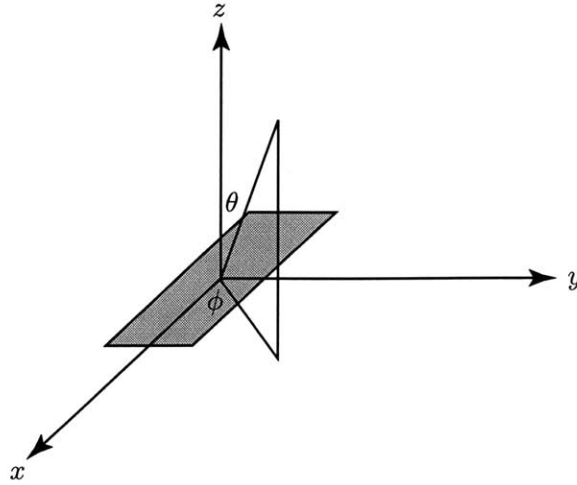
Figure 5-3: Orientation of the incident wave

5.2   Square Patches

In this section, the formulation presented in the previous chapter is used to calculate the transmission characteristics of a two layer structure. The geometry of the filter is shown in Figure 5-6. It consists of cascaded 3 cm square patches in a square lattice with periodicity of 6 cm. The spacing between the two screens is also 6 cm. Since the elements are patches instead of apertures, the structure acts as a low pass filter in the base band and as a bandstop filter around the primary resonant frequency.

A TE plane wave with $\theta_i = 0°$ is used as the incident wave, and the effective spectrum is from 0.1 GHz to 10 GHz, which is around twice the fundamental resonant frequency.

The main interest is the transmission of the fundamental mode. When the frequency is smaller than the first resonant frequency, which occurs at approximately $w = \lambda/2$, the interaction is expected to be dominated by the $(0,0)$ mode. But as the frequency goes higher, the high-order modes will start to propagate and will couple
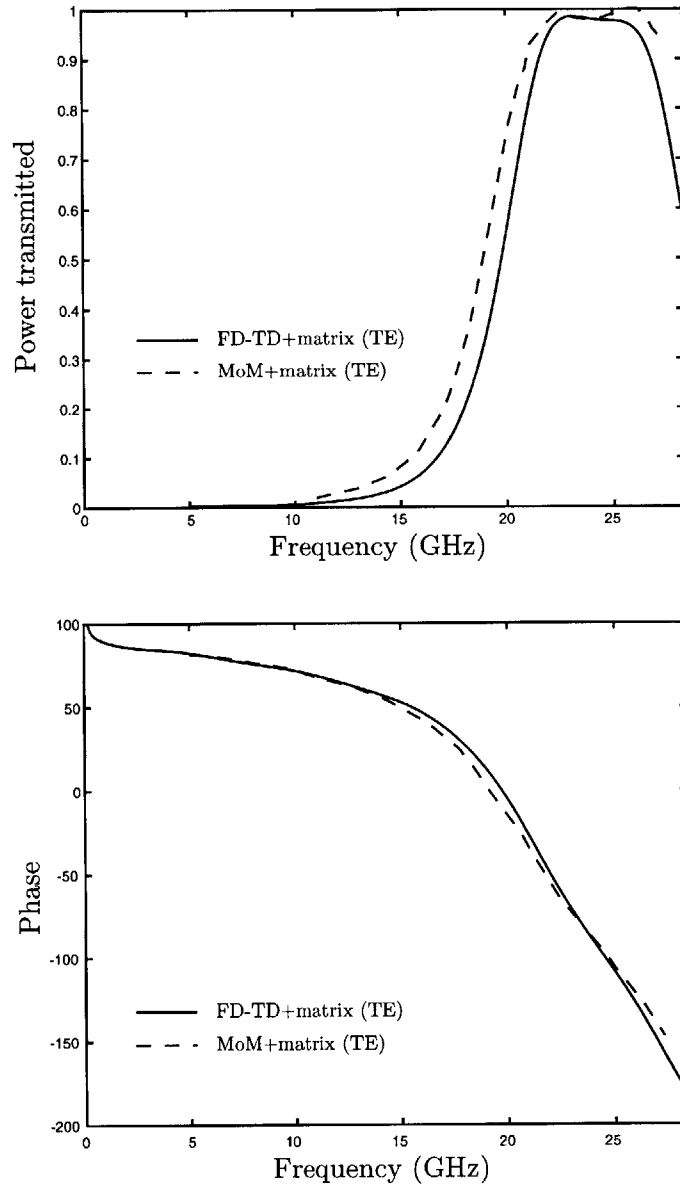
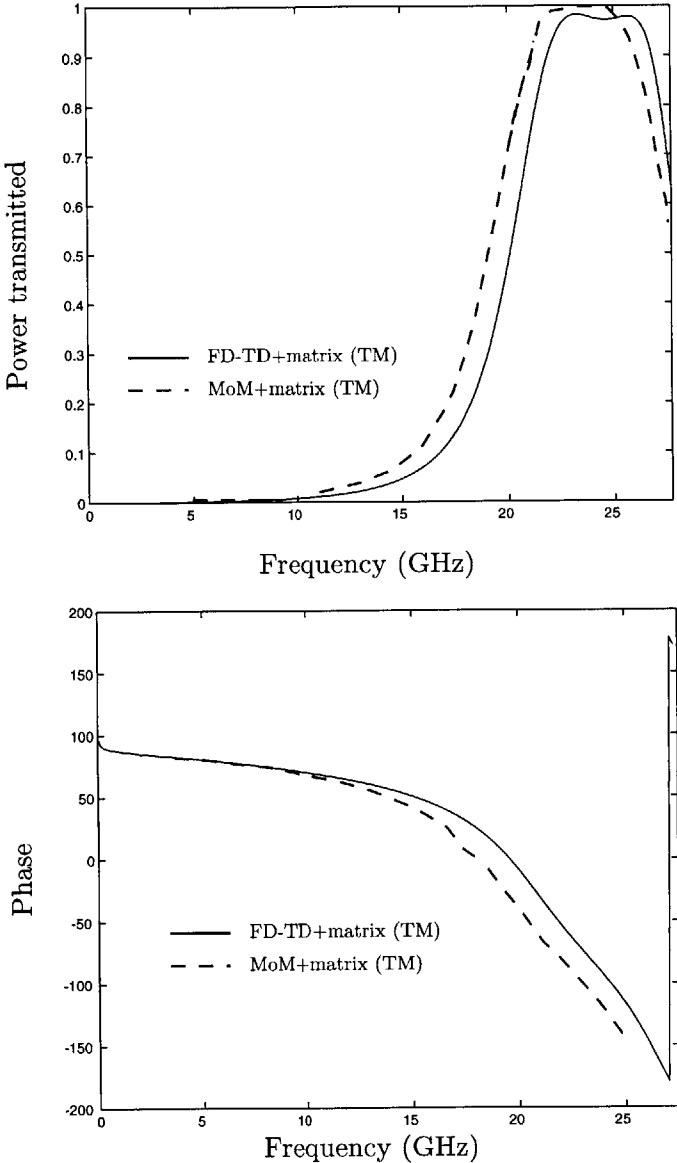Figure 5-4: Comparison between two different hybrid methods for TE incidence.

Figure 5-5: Comparison between two different hybrid methods for TM incidence.

Degenerate modes	Degeneracy
(0,0)	1
(1,0) (-1,0)	2
(0,-1) (0,1)	2
(-1,-1) (-1,1) (1,-1) (1,1)	4

Table 5.1: Degeneracy of modes for normal incidence

back to the fundamental mode. To form a finite generalized scattering matrix, a total of nine modes is included. Since the scattering elements are square patches, several modes are degenerate (Table 5.2), which allows a simpler operation on the scattering matrices.

The magnitude of $e^{ik_z z}$ is plotted against frequency for different modes in Figure 5-7. Since the separation is the same as the center-to-center spacing of the metal element, the effect of evanescent waves is small. The cutoff frequencies of the higher-order modes are useful in interpreting the region in which the higher-order modes are coupled back to the $(0,0)$ mode. The co-polarized transmission coefficients S_{21}^{HH} for different modes are plotted in Figure 5-8. Among the co-polarized modes, $(0,1)$ has the smallest contribution. The cross-polarized transmission coefficients S_{21}^{HV} for different modes are plotted in Figure 5-9, The contributions of the modes are summed up and the comparison is shown in Figure 5-10, where the solid line represents the full-wave FD-TD solution, and the rest are the hybrid method results. The dotted line corresponds to the matrix multiplication of the $(0,0)$ mode term only. It is observed that the transmission below the fundamental resonant frequency is basically determined by only the $(0,0)$ mode. The dash-dotted line represents the $(0,0)$ mode and the coupling between the $(0,0)$ and $(1,0)$ mode, which explains the secondary nulls at around 6 GHz. The last result is the closest when compared to the FD-
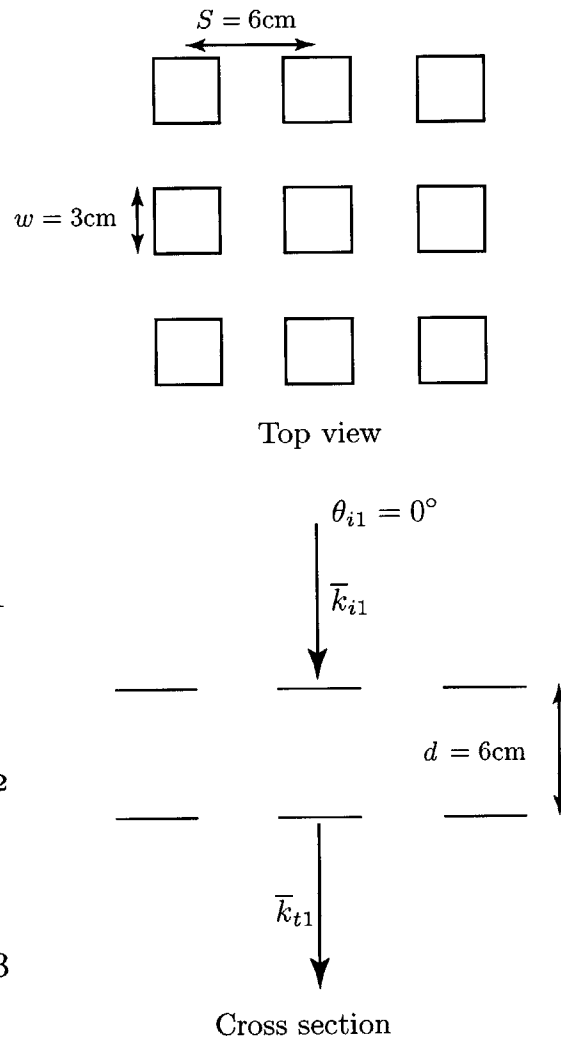
Figure 5-6: Geometry of the cascaded metal screen used in the hybrid method.

TD calculation. The inaccuracy of the hybrid method around the double nulls at around 6.5 GHz may be due to the inaccuracy of the scattering coefficients. As the higher-order modes start to change from evanescent to propagating, the absorbing boundary cannot absorb the grazing incident wave well, and it causes inaccuracies in the calculation of the coefficients.

Figure 5-7: Magnitude of vertical propagation factor for different modes.

Figure 5-8: Transmission coefficients of different modes (co-polarized).

Figure 5-9: Transmission coefficients of different modes (cross-polarized).

Figure 5-10: Comparison between FD-TD and hybrid method.
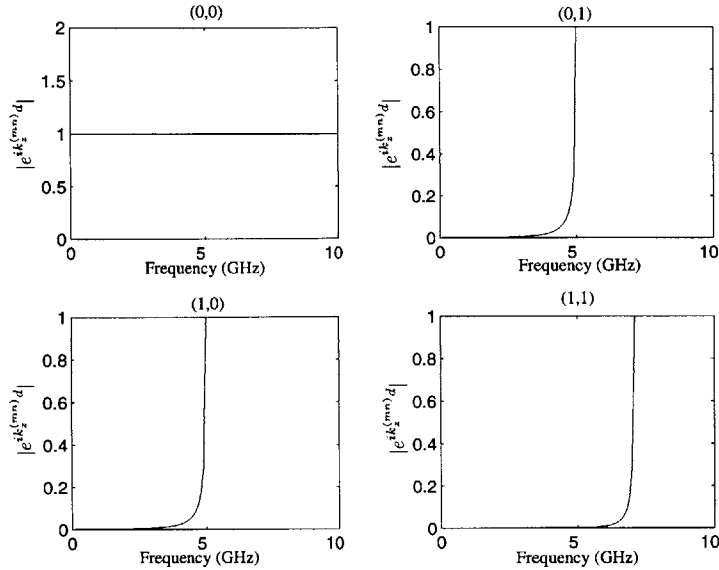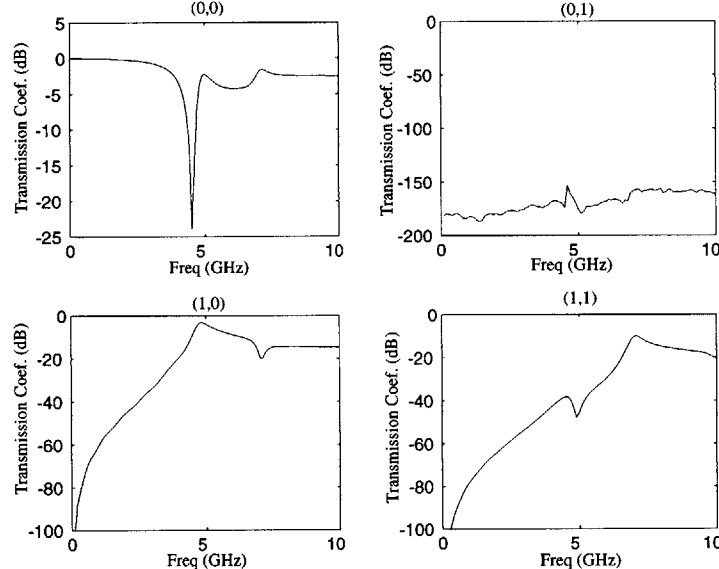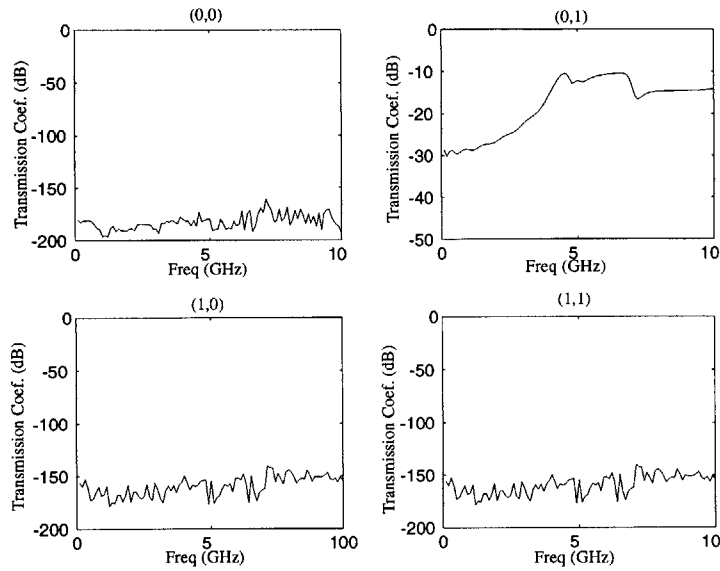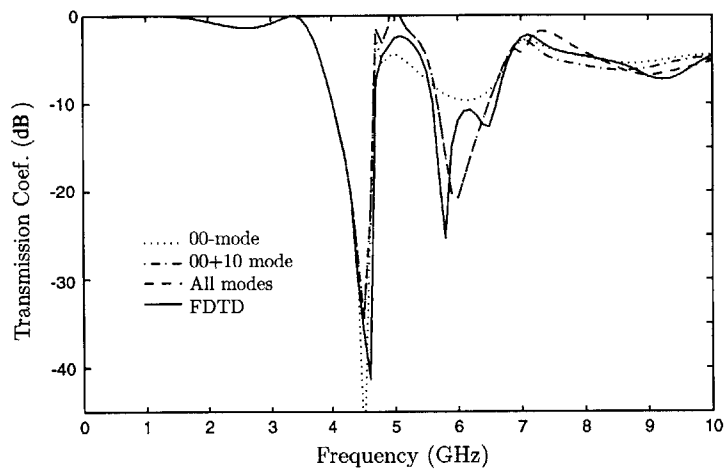
Chapter 6

Conclusion

In this thesis the oblique incidence Finite-Difference Time-Domain technique for periodic surfaces is used to calculate the transmission characteristics of an infrared bandstop photonic crystal filter. The relation between the bandwidth and filling percentage of the unit cell is studied by the variation of parameters. The mechanisms of the dual stopbands are investigated. The separation between the layer and the relative size of the metal patches determines the position and bandwidth of the lower stopband, and the periodicity across the same surface determine the position of the upper stopband. A higher metal filling percentage also enhances the bandwidth. The knowledge gained is used to design a bandstop filter at the band $3 - 5\,\mu$m and $8 - 12\,\mu$m. The final design features a stopband with transmission coefficients below -10 dB for the major polarization from an incident angle of $0°$ to $\pm60°$ for the band $8 - 12\,\mu$m and a partial stopband for the $3 - 5\,\mu$m band.

Using FD-TD in conjunction with a transfer matrix method, a hybrid method is employed to study the effects of higher-order interaction within photonic crystal bandstop filters. Using a generalized scattering matrix and transforming it into a transfer matrix the effects of individual modes can be studied and analyzed. It is

found that, for a multilayer filter, though the propagation of the fundamental mode is straightforward below the first resonant frequency, the propagation of higher-order modes can couple back to the fundamental mode for high frequency and can not be neglected. The same approach is used for the oblique incidence case, in which the inclusion of higher-order modes improves the accuracy for high frequencies.

Symmetries of the filter are exploited to facilitate the computation of the matrix elements. For normal incidence, the degeneracies of different modes are more pronounced while for oblique incidence, symmetries can be found only on both sides of the incidence planes.

Future work should include the analysis of very close coupling of the filter element and capturing of the evanescent waves in the FD-TD computational domain. Since the evanescent waves decay exponentially, an exponential discretization over the surface of the filter may allow more accurate calculation of the amplitudes of the matrix elements.

A better absorbing boundary can eliminate the reflection of incident waves at grazing angles which happen at the transition when a mode turns from evanescent to propagating. The present boundary creates reflected waves at the transitional frequencies and may give rise to inaccurate scattering coefficients.

An improvement of the coefficient calculation may also help to enhance the resolving power of the hybrid method and reveal the finer details which for now are captured only by the full-wave method.

Bibliography

[1] J. D. Joannopoulos, R. D. Meade, and J. N. Winn, *Photonic Crystals*, Princeton University Press, 1995.

[2] E. Yablonovitch, "Photonic band-gap crystals," *J. Physics-Condensed Matter*, vol. 5, no. 16, pp. 2443–2460, Apr. 1993.

[3] S. Fan, "Photonic crystals: Theory and device applications," M.S. thesis, Massachusetts Institute of Technology, 1997.

[4] K. A. McIntosh, L. J. Mahoney, K. M. Molvar, O. B. McMahon, S. Verghese, M. Rothschild, and E. R. Brown, "Three-dimensional metallodielectric photonic crystals exhibiting resonant infrared stop bands," *Appl. Phys. Lett.*, vol. 70, no. 22, pp. 2937–2939, June 1997.

[5] P. H. Siegel, R. J. Dengler, and J. C. Chen, "THz dichroic plates for use at high angles of incidence," *IEEE Microwave & Guided Wave Lett.*, vol. 1, no. 1, pp. 8–9, Jan. 1991.

[6] A. Kao, K. A. McIntosh, O. B. McMahon, A. R. Atkins, and S. Verghese, "Calculated and measured transmittance of metallodielectric photonic crystals incorporating flat metal elements," *Appl. Phys. Lett.*, vol. 73, no. 2, pp. 145–147, July 1998.

[7] R. Ulrich, "Far-infrared properties of metallic mesh and its complementary structure," *Infrared Physics*, vol. 7, pp. 37–55, 1967.

[8] C. C. Chen, "Transmission of microwave through perforated flat plates of finite thickness," *IEEE Trans. Microwave Theory Tech.*, vol. MTT-21, no. 1, pp. 1–6, Jan. 1973.

[9] J. N. Winn, Y. Fink, S. Fan, and J. D. Joannopoulos, "Omnidirectional reflection from a one-dimensional photonic crystal," *Optics Letters*, vol. 23, no. 20, pp. 1573–1575, Oct. 1998.

[10] M. E. Veysoglu, R. T. Shin, and J. A. Kong, "A finite-difference time-domain analysis of wave scattering from periodic surfaces: oblique incidence case," *J. Electromagnetic Waves and Applications*, vol. 7, no. 12, pp. 1595–1607, 1993.

[11] A. Kao, "Finite-difference time-domain modeling of oblique incidence scattering from periodic surfaces," M.S. thesis, Massachusetts Institute of Technology, 1997.

[12] R. E. Collin, *Foundations for Microwave Engineering*, McGraw-Hill, Inc., New York, second edition, 1992.

[13] K. S. Yee, "Numerical solution of initial boundary value problems involving Maxwells's equations in isotropic media," *IEEE Trans. Antennas Propagat.*, vol. AP-14, no. 3, pp. 302–307, May 1966.

[14] A. Taflove, *Computational Electrodynamics: The Finite-Difference Time-Domain Method*, Artech House, Boston, 1995.

[15] J. P. Berenger, "A perfectly matched layer for the absorption of electromagnetic waves," *J. Comp. Phys.*, vol. 114, pp. 185–200, 1994.

[16] J. A. Kong, *Electromagnetic Wave Theory*, John Wiley & Sons, Inc., New York, second edition, 1990.

[17] T. A. Cwik and R. Mittra, "The cascade connection of planar periodic surfaces and lossy dielectric layers to form an arbitrary periodic screen," *IEEE Trans. Antennas Propagat.*, vol. AP-35, no. 12, pp. 1397–405, Dec. 1987.

[18] R. C. Hall, R. Mittra, and K. M. Mitzner, "Analysis of multilayered periodic structures using generalized scattering matrix theory," *IEEE Trans. Antennas Propagat.*, vol. AP-36, no. 4, pp. 511–517, Apr. 1988.

[19] C. Wan and J. A. Encinar, "Efficient computation of generalized scattering matrix for analyzing multilayered periodic structures," *IEEE Trans. Antennas Propagat.*, vol. AP-43, no. 11, pp. 1233–1242, Nov. 1995.

[20] T. A. Cwik and R. Mittra, "Scattering from a periodic array of free-standing arbitrarily shaped perfectly conducting or resistive patches," *IEEE Trans. Antennas Propagat.*, vol. AP-35, no. 11, pp. 1226–1234, Nov. 1987.

[21] J. C. Vardaxoglou, *Frequency Selective Surfaces*, Research Studies Press Ltd., 1997.

[22] G. Manara, A. Monorchio, A. Talarico, and R. Mittra, "Design of a dichroic surface for dual-frequency radioastronomical observation," *Microwave Opt. Technol. Lett.*, vol. 20, no. 2, pp. 126–129, Jan. 1999.

[23] K. A. McIntosh, O. B. McMahon, and S. Verghese, "Three-dimensional metallodielectric photonic crystals incorporating flat metal elements," *Microwave Opt. Technol. Lett.*, vol. 17, no. 3, pp. 153–156, Feb. 1998.

[24] D. F. Sievenpiper, M. E. Sickmiller, and E. Yablonovitch, "3D wire mesh photonic crystals," *Phys. Rev. Lett.*, vol. 76, no. 14, pp. 2480–2483, Apr. 1996.

[25] C. C. Cheng, V. Arbet-Engels, A. Scherer, and E. Yablonovitch, "Nanofabricated three dimensional photonic crystals operating at optical wavelengths," *R. Swedish Acad. Sci. Physica Scripta*, vol. T68, pp. 17–20, 1996.

[26] E. A. Parker and S. M. A. Hamdy, "Rings as elements for frequency selective surfaces," *Electronics Letters*, vol. 17, no. 17, pp. 612–614, Aug. 1981.

[27] J. A. Kong, "Second-order coupled-mode equations for spatially periodic media," *J. Opt. Soc. Am.*, vol. 67, no. 6, pp. 825–829, June 1977.

[28] S. W. Lee, G. Zarrillo, and C. L. Law, "Simple formulas for transmission through periodic metal grids or plates," *IEEE Trans. Antennas Propagat.*, vol. AP-30, no. 5, pp. 904–909, Sep. 1982.

[29] J. A. Arnaud and F. A. Pelow, "Resonant-grid quasi-optical diplexers," *Bell System Technical Journal*, vol. 54, no. 2, pp. 263–283, Feb. 1975.

[30] D. F. Sievenpiper, E. Yablonovitch, J. N. Winn, S. Fan, P. R. Villeneuve, and J. D. Joannopoulos, "3D metallo-dielectric photonic crystals with strong capacitive coupling between metallic islands," *Phys. Rev. Lett.*, vol. 80, no. 13, pp. 2829–2832, Mar. 1998.

[31] D. W. Porterfield, J. L. Hesler, R. Densing, E. R. Mueller, T. W. Crowe, and R. M. Weikle II, "Resonant metal-mesh bandpass filters for the infrared," *Appl. Optics*, vol. 33, no. 25, pp. 6046–6052, Sep. 1994.

[32] B. J. Rubin and H. L. Bertoni, "Reflection from a periodically perforated plane using a subsectional current approximation," *IEEE Trans. Antennas Propagat.*, vol. AP-31, no. 6, pp. 829–836, Nov. 1983.

[33] P. Yeh, A. Yariv, and C.-S. Hong, "Electromagnetic propagation in periodic stratified media," *J. Opt. Soc. Am.*, vol. 67, no. 4, pp. 423–438, Apr. 1977.

[34] T. Schimert, M. E. Koch, and C. H. Chan, "Analysis of scattering from frequency-selective surfaces in the infrared," *J. Opt. Soc. Am. A*, vol. 7, no. 8, pp. 1545–1553, Aug. 1990.

[35] S. Fan, P. R. Villeneuve, and J. D. Joannopoulos, "Large omnidirectional band gaps in metallodielectric photonic crystals," *Phys. Rev. B*, vol. 54, no. 16, pp. 11245–11251, Oct. 1996.

[36] J. P. Montgomery, "Scattering by an infinite array of multiple parallel strips," *IEEE Trans. Antennas Propagat.*, vol. AP-27, no. 6, pp. 798–807, Nov. 1979.

[37] A. S. Barlevy and Y. Rahmat-Samii, "Analysis of arbitrary frequency selective surfaces: analytic constraints," in *IEEE Trans. AP-S Int. Symp. Dig.*, Baltimore, MD, July 1996, vol. 2, pp. 1440–1443.

[38] S. M. A. Hamdy, "Modal analysis of periodic arrays of simple and concentric rings as elements for frequency selective surfaces," in *URSI National Radio Science Symposium on Electromagnetic Waves*, Cairo, Egypt, Feb. 1983, pp. 115–131.

[39] A. Scherer, C. C. Cheng, O. Painter, J. O'Brien, A. Yariv, E. Yablonovich, and V. Arbet-Engels, "Microfabrication of photonic bandgap crystals," in *23rd International Conference on the Physics of Semiconductors*, Berlin, Germany, July 1996, vol. 4, pp. 3063–3069.

[40] C. Wan and J. A. Encinar, "Exploitation of symmetries in the impedance matrix for moment-method analysis of arbitrary frequency-selective surfaces," in *IEEE Trans. AP-S Int. Symp. Dig.*, Newport Beach, CA, June 1995, vol. 3, pp. 1648–1651.

[41] T. K. Wu, *Frequency Selective Surface and Grid Array*, Wiley & Sons, New York, 1995.